Intracellular pocket conformations determine signaling through the μ opioid receptor

David A. Cooper,[1] Joseph DePaolo-Boisvert,[1] Stanley A. Nicholson,[2] Barien Gad,[2,3] David D. L. Minh[1,3]*

[1]Department of Chemistry, [2]Department of Applied Mathematics, [3]Department of Biology, Illinois Institute of Technology; Chicago, United States of America.

*Corresponding author. Email: dminh@iit.edu

Summary

The relationship between the binding of a ligand to a receptor and activation of biological signaling pathways has remained unclear. The challenge is compounded by functional selectivity, in which a single ligand binding to a single receptor can activate multiple signaling pathways at different levels[1]. Spectroscopic studies show that in the largest class of cell surface receptors, 7 transmembrane receptors, activation is associated with shifts in the equilibria of intracellular pocket conformations[2,3]. We hypothesized that signaling through the μ opioid receptor, a prototypical 7TMR, is linearly proportional to the equilibrium probability of observing intracellular pocket conformations. Here we show that a machine learning model based on this hypothesis accurately calculates the efficacy of both G protein and β-arrestin-2 signaling. Structural features that the model associates with activation are intracellular pocket expansion, toggle switch rotation, and sodium binding pocket collapse. Distinct pathways are activated by different arrangements of the ligand and sodium binding pockets and the intracellular pocket. Our study provides the first evidence for what could be a scientific law. While recent work has

categorized ligands as active or inactive (or partially active) based on binding affinities to two conformations[4,5], our approach accurately computes signaling efficacy along multiple pathways.

Introduction

Cell surface receptors transduce extracellular signals into multiple intracellular pathways. Remarkably, in a phenomenon known as functional selectivity[1] or biased signaling, a single ligand binding to a single receptor can have different effects on distinct signaling pathways. In the largest class of cell surface receptors, 7 transmembrane helix receptors (7TMRs) (also known as G-protein coupled receptors), ligands can differentially activate or inhibit pathways involving heterotrimeric G proteins, 7TMR kinases, and β-arrestins. Signaling efficacy (E_{max} from concentration-response curves) quantifies the extent of pathway activation at a saturating concentration of ligand. Some 7TMR ligands are balanced, with comparable efficacy for both G protein and β-arrestin pathways; others are biased, with much higher efficacy for one class of pathways. While 7TMRs are particularly useful targets for drugs ("druggable"), targeted by approximately one third of drugs in the clinic[6], most of these drugs were designed assuming that they would be balanced[1]. As inappropriate pathway modulation may cause adverse side effects, optimizing functional selectivity is likely to produce safer and more effective drugs targeting 7TMRs[7–10] and other signaling proteins.

The tragic history of synthetic opioids starkly illustrates the importance of functional selectivity. Fentanyl and its derivatives block pain, exhibiting their analgesic effects by binding to a 7TMR, the μ opioid receptor (μOR). Although the precise pathways are still debated, adverse side effects of tolerance and respiratory depression are also mediated through the μOR[11–13]. The medicinal chemists who designed the first synthetic opioids reasoned that compounds with high analgesic potency would be safer than morphine[14]. They touted the high binding affinity of

sufentanil to the μOR[15]. Unfortunately, the hypothesis that potent compounds would be safe was incorrect; due to their dangerous side effects, synthetic opioids have become the leading cause of drug overdose deaths in the United States[16]!

Increased recognition of the importance of functional selectivity has inspired extensive research into its mechanisms[1]. The focus of the present paper is on ligand-mediated functional selectivity. This type of functional selectivity is independent of mutation or differential splicing of the receptor or differential expression of transducer elements or downstream effectors[1]. The mechanism of ligand-mediated functional selectivity is generally believed to be stabilization of intracellular pocket conformations that differentially interact with proteins that transduce signals further downstream[2,17].

Spectroscopic methods show that different classes of ligands have different effects on 7TMR conformational dynamics[17]. Wingler et. al. used double electron-electron resonance spectroscopy to show that ligands with different levels of bias can induce at least four sets of conformations of the angiotensin II type 1 receptor[18]. For the β2 adrenergic receptor, nuclear magnetic resonance (NMR) and single-molecule fluorescence have demonstrated that balanced versus biased ligands have different effects on receptor conformational exchange[19,20]. Cong et. al. applied NMR to the μOR to show that biased, unbiased, and partial agonists stabilize different conformations of the receptor[21]. While spectroscopic methods demonstrate the existence of multiple conformations, they have not identified specific three-dimensional structures or determined the extent to which they activate signaling along different pathways.

High-resolution structures provide detailed information about a limited subset of intracellular pocket conformations. X-ray crystallography and cryo-EM structures of 7TMRs are typically solved in complexes that comprise stabilizers, such as antibodies and transducers. These

restrict conformational heterogeneity, making structures easy to solve but also obscuring activation mechanisms. μOR structures have been solved as complexes with 17 different ligands[22] with multiple distinct chemical scaffolds and classes of signaling activity[23]. Even though there are a variety of ligands, receptor conformations fall into only two categories: active, for structures complexed to G proteins; and inactive, for structures complexed to antagonists. Presumably the former are capable of G protein signaling while the latter do not activate signaling along any pathway. Two agonist-bound structures of the closely-related δ opioid receptor[24] may be categorized as intermediate[22]; they feature outward rotations of helix 5 and 6 and inward rotation of helix 7 indicative of 7TMR activation[25], but the tip of helix 6 is less tilted than in the active structures of the μ and κ opioid receptors[24]. Another 7TMR, the angiotensin II type 1 receptor, has been crystallized in distinct active conformations in complex with balanced versus biased ligands[3]. These notable exceptions show that is it difficult to capture unique intracellular pocket conformations in high-resolution structures of 7TMRs.

Molecular dynamics simulations (MDS) reveal additional 7TMR conformations. Distinct intracellular pocket conformations have been observed in simulations of μOR complexes with a wide variety of ligands[21,26–29]. We hypothesized that signaling efficacy is linearly proportional to the equilibrium population of these intracellular receptor conformations. To test this hypothesis, we first performed simulations of μOR complexed with 11 ligands from a variety of chemical series, comprising the most comprehensive set of agonists in a single study to date (previous studies[21,26–29] included up to 5 complexes). We tested this hypothesis by developing a machine learning model that categorizes configurations from MDS into conformations. Fractions of simulation time in each conformation, which are estimates of equilibrium probability, were used

as independent variables for multiple linear regression. Model outputs were signaling efficacies along G protein and β-arrestin pathways.

Results

Efficacy from conformer populations

Model predictions of E_{max} are accurate and precise (Fig. 1). Compared to median experimental values, the efficacy of G protein and β-arrestin-2 pathways is predicted with a mean absolute error of 8.1% and 18.4% and a root mean squared error of 10.8% and 21.2%, respectively. The coefficients of determination (R^2) are 0.67 and 0.69, respectively. The standard deviation of efficacy predictions is small, a demonstration that the training procedure is robust.

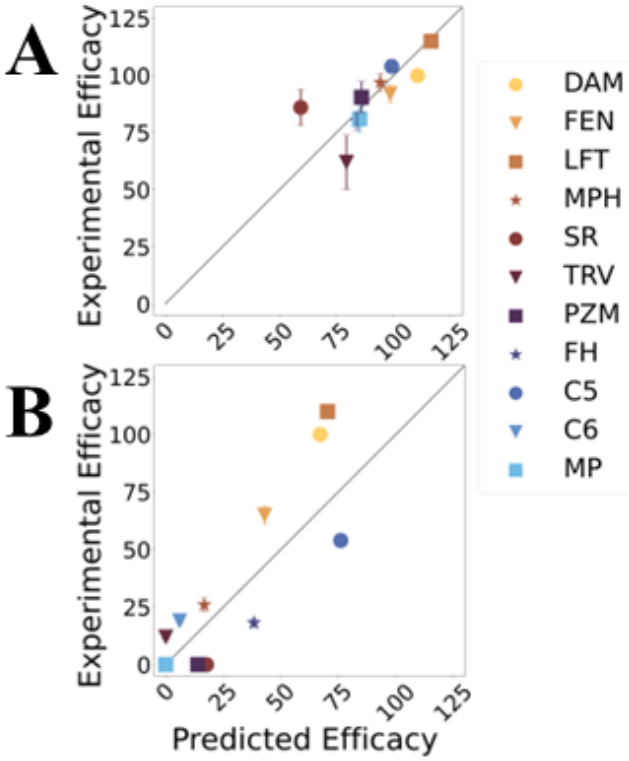

Figure 1 Accuracy of signaling efficacy predictions of ligands for (**A**) G protein and (**B**) β-arrestin-2 pathways. Efficacies are percentages relative to DAMGO. On the x axis, each predicted

efficacy is based on a model trained using all other ligands. The error bar is the standard deviation across 11 cross validation models. On the y axis, each experimental efficacy is the median of reported values listed in Table S1. Error bars are standard deviations of these values. Abbreviations: DAM: DAMGO, FEN: fentanyl, LFT: lofentanil, MPH: morphine, TRV: TRV130, SR: SR17018, PZM: PZM21, FH: FH210, C5: c5guano, C6: c6guano, MP: mitragynine pseudoindoxyl.

The model is based on 14 conformations with a wide range of activity (Fig. 2). We indexed these conformations in decreasing order by average regression slope along G protein and β-arrestin-2 pathways; conformation 1 has the largest average slope and conformation 14 the smallest. However, the average oversimplifies the activity of these conformations. Conformations 4 and 9 promote G protein signaling and repress β-arrestin-2 signaling. Conformations 2, 3, 5, and 7 promote β-arrestin-2 signaling at different levels but have minimal effect on G protein signaling. Conformations 1 and 6 recruit both G proteins and β-arrestin-2. The remaining conformations repress signaling.

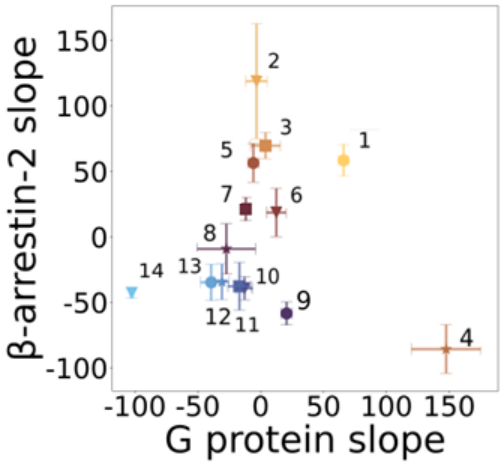

Figure 2 Multiple linear regression slopes of each conformation. The mean (markers) and standard deviation (error bars) are of slopes across all 11 cross validation models.

121 Simulations with different ligands access different ratios of these shared conformations
122 (Fig. S1). Some simulations, such as the apo system (conformation 11) and the complex with
123 DAMGO (conformation 4), are dominated by a single conformation. Others, such as simulations
124 of complexes with PZM21, c5guano, and c6guano, are spread across two or more conformations.
125 Complexes with comparable ligands primarily access distinct conformations, explaining
126 differences in efficacy. Complexes with fentanyl and lofentanil both access conformation 6, but it
127 is not the most populated conformation of either. Similarly, conformation 8 is shared between
128 complexes with both c5guano and c6guano, but both complexes are dominated by other
129 conformations.

130 Most conformations are accessed in simulations with multiple ligands (Fig. S2). However,
131 there are three conformations that are unique to complexes with a specific ligand: 2 (lofentanil),
132 12 (fentanyl), 13 (FH210).

133 *Structural changes and signaling*

134 We defined several functions to help us understand the relationship between structural
135 features and receptor activation (see Materials and Methods). The efficacy response function
136 (ERF) is a sum of estimated probability density functions of a structural feature weighted by linear
137 regression slopes. The general and selective activation scores quantify whether the ERF is
138 significant in both or only one of G protein and β-arrestin-2 recruitment.

139 Activation is associated with rearrangement of helices in the intracellular pocket (Fig. 3A).
140 We use Ballesteros-Weinstein nomenclature[30] in which superscripts describe transmembrane helix
141 (TM) or intracellular loop (ICL), followed by the position relative to the most conserved residue.
142 In structures that favor activation, the intracellular end of TM5 is bent closer to TM1, such that the
143 $G84^{1.46}$-$R260^{5.64}$ distance is reduced by 2 to 4 Å (Fig. S3A). TM6 is pushed outwards away from

TM1, increasing the V91$^{1.53}$-F291$^{6.30}$ and T99^{ICL1}-F291$^{6.30}$ distances (Fig. S3BC). A kink above a proline in TM7 becomes stronger such that the Y328$^{7.43}$-E343^{H8} distance is reduced (Fig. S3F). Compared to β-arrestin-2 activation, G protein activation is favored when TM5 and TM6 are bent further outward relative to helix 8 (Fig. 3B, Fig. S4).

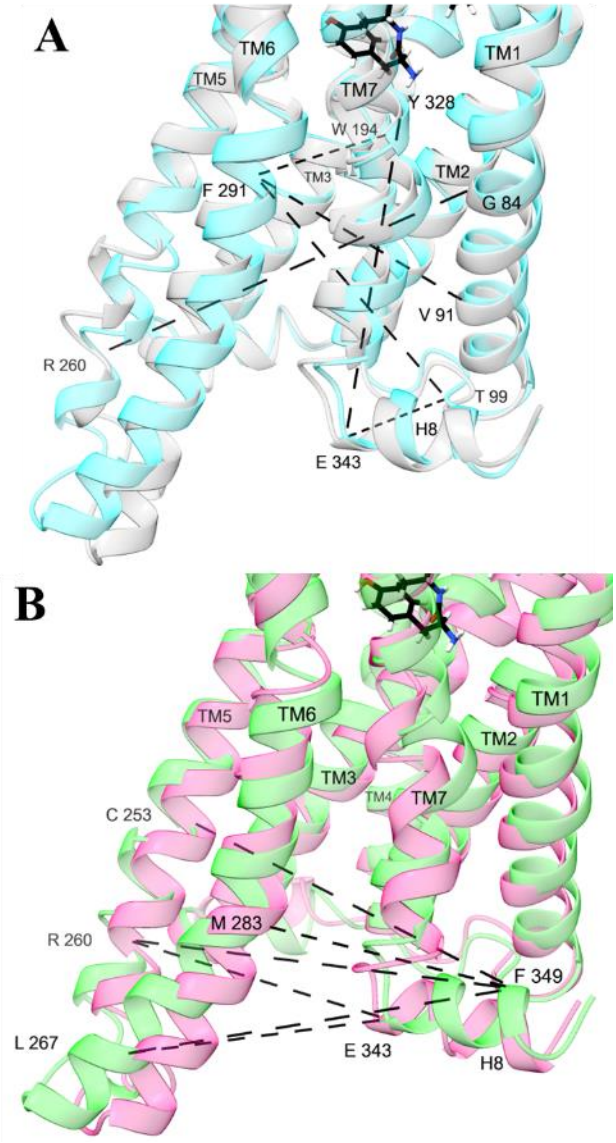

Figure 3 Alpha carbon distances with the largest (A) general and (B) selective activation scores. Structures are medoids of conformations from the machine learning model, colored by

different types of activity: high (cyan, conformation 1), low (grey, conformation 14), G protein (green, conformation 4), and β-arrestin-2 (pink, conformation 2). They are shown from the membrane perspective facing the intracellular pocket. Dashed lines are between atoms are shown for the top 2% of activation function scores. For a full table of general and selective activation scores for alpha carbon distances, see Fig. S5.

Activation is also associated with side chain dihedral angles of several amino acid residues in the orthosteric binding pocket (Fig. 4, Fig. S6). In W295$^{6.48}$, activation relates to a shift in the χ_2 angle from around -120° to around 120° (Fig. S6J), rotating the indole ring towards the intracellular pocket. Across the binding pocket, D149$^{3.32}$, Y150$^{3.33}$, and N152$^{3.35}$ have distinct active and inactive conformations. In active conformations, the carboxylate of D149$^{3.32}$ and the phenol of Y150$^{3.33}$ extend across the binding pocket towards TM5 and TM6. In contrast, D149$^{3.32}$ tucks towards TM2 and Y150$^{3.33}$ extends back towards TM4 in inactive conformations. The orientation of N152$^{3.35}$ coincides with D149$^{3.32}$ and Y150$^{3.33}$, pointing the side chain amide further away from the center of the receptor in active conformations (Fig. 4A). D149$^{3.32}$ and Y150$^{3.33}$ also have high selective activation scores; in G protein selective conformations, the side chains of these residues are further oriented towards a sub pocket of the binding site between TM3, TM4, and TM5 (Fig. 4C).

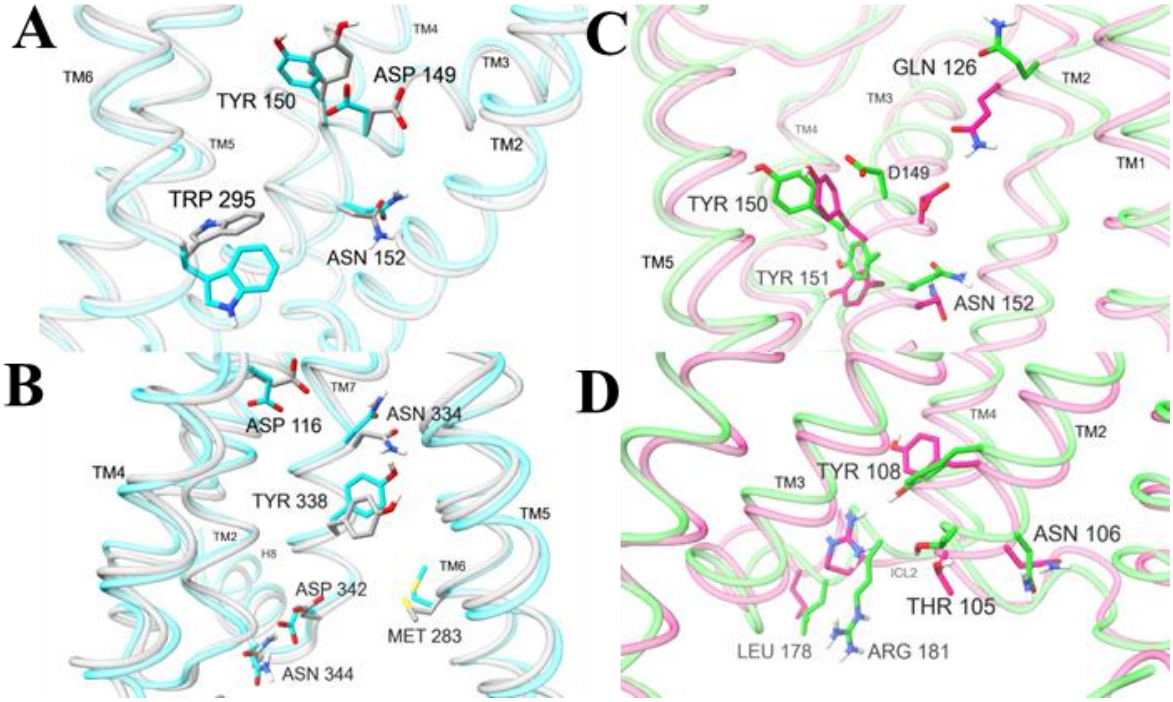

Figure 4 Amino acid positions containing dihedral angles with the highest general and selective activation scores. Structures are medoids of conformations from the machine learning model, colored by different types of activity: high (cyan, conformation 1), low (grey, conformation 14), G protein (green, conformation 4), and β-arrestin-2 (pink, conformation 2). Displayed amino acids contain dihedral angles in the top two percent of general (**A**, **B**) activation scores or (**C**, **D**) selective activation scores. Side chain rotations were adjusted to match the degree with the highest value of the (A, B) general or (C, D) selective activation function. Views of the binding pocket (A, C) are from the perspective behind the binding pocket region of TM7. TM1 and TM7 (A) and TM6 and TM7 (C) were removed to improve the display of binding pocket amino acids. Views of the intracellular region are from the perspective behind TM3 (B) and TM7 (D). TM3 (B), TM6 and TM7 (D) are removed to clearly display the intracellular amino acids. A comprehensive table of general activation and selective activation function scores for analyzed residues are shown in Fig. S9 and 10, respectively.

183 Several residues in the interior of the intracellular pocket also have distinct orientations in
184 active and inactive conformations (Fig. 4, Fig. S6). D116$^{2.50}$ extends down towards intracellular
185 space in active conformations opposed to upwards towards interhelical space in inactive
186 conformations. Along the interior of intracellular TM7, N334$^{7.49}$ and Y338$^{7.53}$ are rotated upwards
187 in active compared to inactive conformations. At the intracellular interface, polar residues
188 M283$^{6.23}$, D342^{H8}, and N344^{H8} assume different side chain configurations in active and inactive
189 conformations.

190 While intracellular pocket side chain dihedrals with large general activation scores are
191 primarily in TM6, TM7, and H8, those with large selective activation scores are across the pocket
192 in ICL2 and TM2 (Fig. 5, Fig. S7). The alcohol group of T105$^{2.39}$ and the amide group of N106$^{2.40}$
193 extend towards ICL2 in G protein selective conformations but towards ICL1 in β-arrestin-2
194 selective conformations. Y108$^{2.42}$ orients across the intrahelical space towards TM3 in β-arrestin-
195 2 selective conformations but downwards towards intracellular space in G protein selective
196 conformations. On ILC2, R181^{ICL2} reaches into intracellular space in the G protein selective
197 conformations but is retracted into the receptor in β-arrestin-2 selective conformations,
198 accompanied by different configurations of nearby L178^{ICL2}.

199 Polar networks in the sodium binding pocket are important both for general and selective
200 activation. The network in this region includes distances between polar atoms of residues D116$^{2.50}$,
201 N330$^{7.45}$, and N334$^{7.49}$ (Fig. 5). Two distances of ~3 and ~4 Å between the first carboxylate atom
202 (OD1) of D116$^{2.50}$ and the nitrogen atom (ND2) of the amide side chain in N334$^{7.49}$ are correlated
203 with general activation. The distance between the second carboxylate atom (OD2) of D116$^{2.50}$ and
204 the nitrogen atom (ND2) of the amide side chain of N330$^{7.45}$ differs in G protein (peaked around
205 ~5.5 Å) opposed to β-arrestin-2 signaling (peaked around ~6.5 Å) (Fig. S11). It is also noteworthy

206 that the neighboring residues W295$^{6.48}$ and N152$^{3.35}$ have dihedral angles with large general
207 activation scores (Fig. S6).

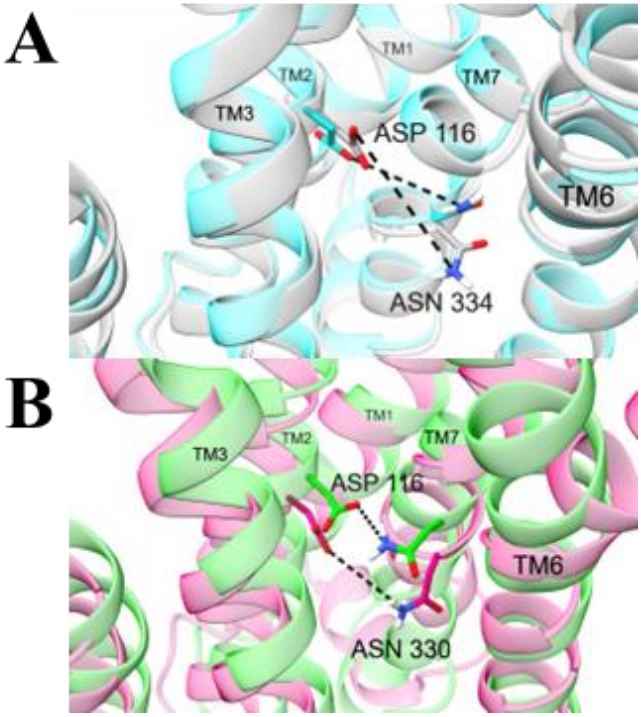

208

209 **Figure 5 Distances in the sodium binding pocket with the highest general and selective**
210 **activation scores.** Structures are medoids of conformations from the machine learning model. (**A**)
211 Distances between OD1 of D116$^{2.50}$ and ND2 of N334$^{7.49}$ in structures with high (cyan,
212 conformation 1) and low (grey, conformation 14) activity. (**B**) Distances between OD2 of D116$^{2.50}$
213 and ND2 of N330$^{7.49}$ in conformations with high G protein (green, conformation 4) and β-arrestin-
214 2 (pink, conformation 2) activity. TM5 is removed to improve display of amino acid distances in
215 the sodium binding pocket. A comprehensive listing of general activation and selective activation
216 function scores for analyzed polar residue distances is shown in Fig. S10.

217

Discussion

Efficacy of μOR conformations

The accuracy of our model (Fig. 1) supports the hypothesis that signaling efficacy is proportional to the equilibrium probability of observing intracellular pocket conformations. In analyzing MDS of the angiotensin II type 1 receptor, Suomivuori et. al. showed that the agonist-bound receptor can transition between two active conformations that are common across complexes with different ligands[31]. One of the active conformations accommodates both G proteins and β arrestins, but the other favors β arrestin binding. They found that the fraction of simulation time spent in each conformation was related to whether the bound ligand was balanced or biased towards one class of pathways. They also observed three other conformations and speculated about their signaling profiles. We have built upon the concept of multiple conformations with distinct signaling profiles to develop a quantitative model that predicts signaling efficacy.

To our knowledge, we have presented the first computational model that connects conformational equilibria to functional selectivity. There have been two recent attempts to use MDS to categorize functional response without regard to the pathway. Panel et. al. computed relative binding free energies between 23 ligands and active and inactive conformations of the β2 adrenoceptor[4]. The calculated shift in binding affinity was used to successfully classify the compounds as agonists, partial agonists, or antagonists. In another study, a team from the computational chemistry software company Schrödinger performed absolute binding free energy calculations of ligands to active and inactive conformations of 7TMR and nuclear hormone receptor targets[5]. Based on higher predicted binding affinity to the active conformation, 168 of 180 ligands (93%) could be correctly classified as agonists opposed to antagonists. We have not only categorized functional response as on or off (or partially on) but provided a quantitative prediction

of efficacy and evaluated the ability of different conformations to activate signaling along multiple pathways.

Our model could be improved with a larger and more consistent training set and extended to compute other properties. While additional ligands could lead induce additional conformations, they could also lead to more precise regression slopes. Due to limited availability, not all efficacy data were based on the same assays (Table S2). A model trained on consistent data would likely lead to more accurate efficacy predictions. Other properties that may be proportional to equilibrium populations of intracellular pocket conformations include efficacies of Gα subtypes and parameters of the Black-Leff[32] operational model: the transducer ratio and dissociation constant of the agonist-receptor-transducer complex.

Our results affirm that many intracellular pocket conformations defy simple classification[2,31]. Conformations are not simply active or inactive. Neither are they simply biased towards G protein or β arrestin signaling. Instead, conformations have a broad range of signaling efficacy across multiple pathways (Fig. 2).

While our model identifies conformations and structural features associated with activation, it does not explain how intracellular pocket conformations lead to distinct signaling efficacies. For G proteins, different intracellular pocket conformations may lead to differential recruitment of heterotrimers with distinct Gα subunits. In turn, these Gα subunits have different effects on adenylyl cyclase, altering readouts from the cyclic adenosine monophosphate (cAMP) inhibition assay that is the basis of the model (Table 1). However, this is not the whole story; biosensor assays show that Gα subunits have different signaling efficacies[33]. As ligand-bound conformations do not exactly match those of ternary complexes, binding may perturb the energy

landscape of transducers to alter their activity (e.g. nucleotide exchange) and thereby their signaling efficacies.

Mechanisms of signaling activation

Activation-induced changes in the overall architecture of intracellular pocket conformations predicted by our model are corroborated by previous studies. As we have observed (Fig. 3), high-resolution structures and spectroscopy have shown that activation is favored by expansion of the intracellular recruitment site through rearrangement and bending of the transmembrane helices[2,34,35]. Moreover, our finding that larger distances between TM5/6 and TM7/H8 are associated with G protein bias is consistent with previous simulations[27,36].

Orthosteric binding site features that our model associates with functional selectivity are consistent with the pharmacophore model from Kelly et al.[37] Molecular modeling methods have been used to design several G protein biased ligands[27,29,38,39]. From an analysis of the interactions between functionally selective agonists and the μOR, Kelly et al. proposed a pharmacophore model in which strong interactions with D149$^{3.32}$ and Y328$^{7.43}$ increase the recruitment of β-arrestin, while interactions with Y150$^{3.33}$ (instead of Y328$^{7.43}$) and a weaker interaction with D149$^{3.32}$ decrease β-arrestin recruitment[37]. Based on this insight, Zhuang et al. created G protein selective fentanyl derivatives[27]. Our observation that D149$^{3.32}$ and Y150$^{3.33}$ extend into the binding pocket in active conformations and retract in inactive conformations suggests that ligand interactions with D149$^{3.32}$ and Y150$^{3.33}$ can have an important role in activation (Fig. 4A). Moreover, our observation that D149$^{3.32}$ and Y150$^{3.33}$ point towards the center of the pocket in β-arrestin-2 selective conformations suggest that they form stronger interactions with ligands, as suggested by Kelly et al[37].

Our observations about the sodium binding site and its allostery are consistent with previous studies. The sodium binding site[40], which houses the cation in inactive conformations, comprises D116$^{2.50}$, S156$^{3.39}$, N330$^{7.45}$, S331$^{7.46}$, and N334$^{7.49}$. The site allosterically communicates with the orthosteric site and the intracellular pocket[2,34,40,41]. Ligand-interactions with D149$^{3.32}$ and Y150$^{3.33}$ in the orthosteric site affect the position of the neighboring residue N152$^{3.35}$. In turn, W295$^{6.48}$ and N152$^{3.35}$ form a network with the sodium binding pocket[42]. These previous studies are consistent with our findings that W295$^{6.48}$ and N152$^{3.35}$ are associated with activation (Fig. S6) and that several polar residues that occupy the sodium binding pocket (D116$^{2.50}$, N330$^{7.44}$, and N334$^{7.48}$) adopt different orientations for generally active, inactive, and selectively active conformations (Fig. 4 and 5).

Our analysis predicts behavior of conserved motifs in the μOR that are consistent with previous observations. Three motifs conserved across many 7TMRs – the transmission switch (CWxP from C6.47 to P6.50), toggle switch (NPxxY from N7.49 to Y7.53), and ionic lock (DRY including D3.49, R3.50, and Y5.58) – are widely considered microswitches involved in activation[43]. W295$^{6.48}$ of the transmission switch and N334$^{7.49}$ and Y338$^{7.53}$ of the toggle switch have distinct conformations and large general activation scores (Fig. 5). The rotation of W295$^{6.48}$ has also been associated with activation in other simulations[21,44]. In contrast, DRY motif residues have significantly smaller activation scores (Fig. S9 and 10). While the arginine in the motif typically coordinates to D/E6.30 in other 7TMRs, μOR has a threonine at this position. Thus, the DRY motif cannot form an ionic contact that stabilizes inactive conformations of other 7TMRs.

Our analysis predicts that some residues at the intracellular end of TM2 (T105$^{2.39}$, N106$^{2.40}$, and Y108$^{2.42}$) and ICL2 (L178^{ICL2} and R181^{ICL2}) have distinct configurations in functionally selective conformations. Based on simulations of ternary complexes, Mafi et. al. also proposed

that R181^{ICL2} and T105$^{2.39}$ play a key role in recruitment[36]. The relevance of R181^{ICL2} to G protein signaling and β-arrestin-2-mediated internalization has been validated by mutagenesis[45]. Our analysis suggests that the extension of R181^{ICL2} into cytoplasmic space may increase the affinity for G proteins while higher placement of the polar side chain may improve affinity for β-arrestin-2.

Efficacy prediction in drug design

Drug developers are increasingly pursuing functional selectivity of 7TMRs to maximize therapeutic potential and minimize adverse effects. These efforts have been hindered by limited understanding of the structural mechanisms of functional selectivity and the inability to quantitatively predict signaling along multiple pathways. Our approach addresses both challenges and could help design novel functionally selective agonists for the μOR. It may be a platform technology that can be extended to other pathways, such as G protein subtypes, and other signaling proteins.

Conclusions

Signaling efficacy of the μOR is linearly proportional to the equilibrium population of intracellular pocket conformations. Equilibrium populations may be accurately estimated by molecular dynamics simulations. Suitable definitions of these intracellular pocket conformations may be determined by training a machine learning model. Intracellular pocket conformations have a broad range of signaling efficacy along different pathways. Efficacy response functions and activation scores are effective metrics for identifying structural features associated with general and selective activation. These analyses lead to predicted structural mechanisms for general and selective activation that are supported by previous computational and experimental studies.

330 ## Methods

331 ### Molecular Dynamics Simulation

332 We built three-dimensional models of human μOR in the apo form and bound to various
333 ligands based on experimental structures available in the Protein Data Bank (Table S1). Models
334 were built based on the first chain of the 7TMR that appears in each file, excluding additional
335 7TMR subunits and G proteins. The apo structure was based on the DAMGO-bound structure
336 8EFQ with DAMGO removed. Proteins were protonated with pdb2pqr (version 3.6.1)[46] with a pH
337 of 7.0. Ligands were protonated using RDKit (version 2023.03.1) with a pH of 7.0. Protein-ligand
338 complexes were solvated with 0.15 M NaCl and inserted into a membrane using our group's
339 custom scripts (https://github.com/swillow/pdb2amber). The scripts build a DPPE lipid bilayer
340 around the protein after alpha carbon alignment to a μOR structure (5C1M) in the Orientations of
341 Proteins in Membranes[47] database. Complexes were parameterized using AMBER forcefields
342 ff14SB[48] for the protein, opc3[49] for the water, and lipid17 for the membrane. Ligands were
343 parameterized using the GAFF2 force field from AmberTools (version 22.0)[50].

344 MDS were performed using OpenMM version 8.0.0[51]. The systems were minimized using
345 the local energy minimizer *simtk.openmm.app.simulation.Simulation.minimizeEnergy* with 500
346 kJ/mol/nm^2 restraints on the protein and membrane, 5000 iterations, and a tolerance of 100 kJ/mol.
347 Equilibration was performed in several stages. First, water and membrane were equilibrated with
348 500 picoseconds of NVT simulation with 300 kJ/mol/nm^2 restraints on the protein and z-coordinate
349 positions of the membrane. Next, two cycles of 5 nanosecond NPT simulation were performed,
350 with the first cycle using a Monte Carlo Membrane Barostat and the second using a Monte Carlo
351 Barostat. All equilibration simulation was performed with a time second of 2 femtoseconds at 300
352 K. Integration moves were made using the Langevin Middle Integrator. Production simulations

were performed in triplicate for 500 ns each with a timestep of 3 femtoseconds, saving configurations every 7.5 picoseconds. Production runs were performed at 300 K and 1 bar of pressure with a Monte Carlo Barostat and powered by the Langevin Middle Integrator. Calculations were performed using computing resources provided by the Advanced Cyberinfrastructure Coordination Ecosystem: Services & Support (ACCESS) program[52].

Efficacy Calculations

We developed a machine learning model to compute signaling efficacies. Model inputs were configurations from MDS of complexes with each ligand. Outputs were experimental efficacies curated from the literature (Tables S1 and S2). Experimental data from the cyclic adenosine monophosphate (cAMP) assay, which measures the inhibition of downstream cAMP production, were used for G protein signaling efficacies[53]. For the β-arrestin-2 pathway, we included data from standard assays for measuring β-arrestin-2 recruitment[53]: NanoBit, BRET, PathHunter, and Tango. Assays performed with G protein receptor kinases (GRKs) were excluded.

The model is particularly simple and interpretable, based on multiple linear regression (MLR). First, configurations from MDS are clustered into C conformations. This step yields $f_{l,c}$, the fraction of simulations with ligand l in conformation c. Next, the signaling efficacy is computed based on a weighted sum over all conformations,

$$E_{l,G} = \beta_{G,0} + \sum_{c=1}^{C} \beta_{G,c} f_{l,c}, \quad (1)$$

where $E_{l,G}$ is the signaling efficacy of ligand l and $\beta_{G,n}$ are regression slopes along G protein pathway. Analogous terms for the β-arrestin-2 pathway, $E_{l,\beta}$ and $\beta_{\beta,n}$, are computed via an analogous expression. We used the MLR implementation in the open source python package scikit-learn (version 1.3.0)[54].

The machine learning model has parameters and hyperparameters. The parameters are regression slopes. Once conformations are defined and fractions computed, these are uniquely defined by the least squares solution for a particular set of input populations and output efficacies. However, the process of defining conformations involves hyperparameters (1) for distances between configurations and (2) for clustering.

(1) Distances between configurations

Each sampled configuration was characterized using three vectors of features (Fig. S7): $\vec{\theta}$, the N_θ backbone and side chain torsion angles (ψ, ϕ, χ_1, and χ_2 angles) of all the intracellular protein residues (G84$^{1.46}$-D116$^{2.50}$, S156$^{3.39}$-W194$^{4.50}$, P246$^{5.50}$-F291$^{6.44}$, Y328$^{7.43}$-F349^{H8}); $\vec{C}$, the N_C pairwise distances between alpha carbons from residues in the middle and intracellular end of each helix, with at least one residue in between, and the middle of each intracellular loop (G84$^{1.46}$, V91$^{1.53}$, T99^{ICL1}, K102^{ICL1}, T105$^{2.39}$, D116$^{2.50}$, S156$^{3.39}$, S164$^{3.47}$, A170$^{3.53}$, L178^{ICL2}, P183$^{4.39}$, W194$^{4.53}$ C253$^{5.57}$, R260$^{5.64}$, L267^{ICL3}, K271$^{6.11}$, M283$^{6.23}$, F291$^{6.30}$, Y328$^{7.43}$, Y338$^{7.53}$, G343^{H8}, and F349^{H8}); and $\vec{H}$, the N_H distances between intracellular hydrogen bond donors and acceptors observed to be within 8.0 Å of the first configuration of FH210-bound complex (PDB ID 7SCG)[39]. For each vector, we use the subscript k as an index. The distance between configurations i and j was defined as,

$$D_\Theta(i,j) = \sqrt{\frac{1}{N_\theta}\sum_{k=1}^{N_\theta}\left[180 - \left||\theta_k(i) - \theta_k(j)| - 180\right|\right]^2}, \quad (2)$$

$$D_C(i,j) = \sqrt{\frac{1}{N_C}\sum_{k=1}^{N_C}[C_k(i) - C_k(j)]^2}, \quad (3)$$

$$D_H(i,j) = \sqrt{\frac{1}{N_H}\sum_{k=1}^{N_H}[H_k(i) - H_k(j)]^2}, \quad (4)$$

$$\boldsymbol{D_{ij}} = w_\theta \frac{D_\theta(i,j)}{max(D_\theta(i,j))} + w_C \frac{D_C(i,j)}{max(D_C(i,j))} + w_H \frac{D_H(i,j)}{max(D_H(i,j))} \quad (5)$$

Equation 2 is based on the smallest difference, accounting for periodicity, between torsion angles. Equations 2, 3 and 4 demonstrate how each component was calculated, while equation 5 shows how components are combined to represent a single value for the distance between frames *i* and *j*. The sum of weights was constrained to one, such that $w_\theta + w_C + w_H = 1$.

(2) Clustering

Intracellular conformations were defined by clustering. First, hierarchical clustering with complete linkage was performed using scipy (version 1.11.3)[55] based on pairwise distances calculated from equation 5, leading to *H* hierarchical clusters. Second, the pairwise RMSD between the hierarchical cluster centroids was calculated. The RMSD distance matrix of centroids $\boldsymbol{D_{rmsd}}$ was converted into a similarity matrix $\boldsymbol{S_{rmsd}}$ using a Gaussian function implemented in scikit-learn[54],

$$\boldsymbol{S_{rmsd}} = e^{\frac{-(\boldsymbol{D_{rmsd}})^2}{2\delta^2}}, \quad (6)$$

which introduces a bandwidth hyperparameter δ. Centroids and corresponding configurations were grouped into conformations using spectral clustering from scikit-learn with the *cluster_qr* assignment algorithm. This algorithm uses $\boldsymbol{S_{rmsd}}$ and returns *C* conformations.

Training and Cross-validation

Leave-one-out procedures were used *both* for training and cross-validation. In statistics, cross-validation involves separating the data into a training set and a test set. A machine learning model that does not overfit the data produces accurate outputs not only for the training set, but also for the test set. In leave-one-out cross validation, the test set comprises of one sample and the

training set is the remainder of the data. The training is repeated multiple times with each sample as the test set.

The machine learning model was trained based on a leave-one-out loss function. Each training set was further divided into a sub-test set comprising one sample and sub-training set containing the remainder of the data. Sub-training was repeated multiple times with each training set sample as the sub-test set. The loss function was the mean square error of the sub-test set, averaged over all the sub-training processes for the given training set.

The loss function was optimized via a grid search. Distance components were weighted according $(w_\theta,\ w_C,\ w_H) \in \{(w, w, 1-2w), (w, 1-2w, w), (1-2w, w)\}$, where $w \in \{0.1, 0.2, 0.25, 0.33, 1\}$. Clustering hyperparameters were varied over a range of integers, with the number of clusters H between 2 and 40, the bandwidth δ between 1 and 3, and the number of conformations $C \in \{2, 3, \ldots, H-1\}$. For each combination of hyperparameters, the leave-one-out loss was computed for both G protein and β-arrestin-2 efficacy. Hyperparameters were selected based on minimizing the sum of the leave-out-out loss of both efficacies.

Leave-one-out training led to consistent values of all machine learning hyperparameters. For all 11 models trained with each ligand as the test set, the best performance was observed with the distance weights of $w_\theta = 0.25, w_C = 0.25,$ and $w_H = 0.5$, the number of hierarchical clusters $H = 40$, and bandwidth $\delta = 2$, and the number of conformations C = 14. The consistency of these parameters indicates that the training procedure is robust, insensitive to the inclusion or exclusion of any single ligand. Thus, these hyperparameters were used for all models reported in the paper.

The machine learning model was validated via leave-one-out cross-validation. Reported signaling efficacies and performance metrics are based on these models which do not include test

compounds within training sets. This procedure is consistent with the way efficacy would be predicted for a ligand with a known binding pose but unknown efficacy.

Structural Analysis

To help us understand the relationship between structural features and receptor activation, we defined an *efficacy response function* (ERF) based on the defined conformations and MLR weights from the machine learning model. First, we recorded the slopes from each training iteration of the single conformational space that minimizes the loss function. For each structural feature, we computed a kernel density estimate (KDE) of the probability density function within each conformation using *numpy.histogram*, with the density feature (version 1.26.0)[56]. Each torsional sample Φ was triplicated at $\Phi + 2\pi$ and $\Phi - 2\pi$ to make the density estimate continuous over the period. The KDE was normalized based on evaluating the integral over the range $[-\pi, \pi]$ using *numpy.histogram*, with the density feature (version 1.26.0)[56]. Next, the normalized KDEs were multiplied by corresponding mean MLR slopes and summed together, resulting in efficacy response functions. ERFs were computed for all features that were used to compute distances (see *Distances between configurations*) and for both G protein and β-arrestin-2 activation. ERFs calculations were extended to residues in the binding pocket, which did not contribute to distances, and weighted with the corresponding intracellular configuration.

An ERF helps identify changes in the probability density that favor an activation process. It is important to note that an ERF is not a probability density function. Because MLR slopes may be negative, an ERF can be negative. Moreover, they are not normalized. Nonetheless, ERFs are helpful for interpreting the machine learning model. Shifting a probability density towards a region with high ERF values favors activation. Conversely, shifting a probability density towards a region

with low ERF values favors inactivation. If the ERF is near zero over the entire range, the feature is unrelated to activation.

As we computed many ERFs, we also defined several metrics to help us prioritize, in an unbiased way, which structural features to focus our attention on. We defined the general activation function $a(x)$ as,

$$a(x) = \begin{cases} \min\left(|r_G(x)|, |r_\beta(x)|\right) & if\ \left(r_G(x) > 0\ and\ \ r_\beta(x) > 0\right)\ or\ \left(r_G(x) < 0\ and\ \ r_\beta(x) < 0\right), \\ 0\ otherwise \end{cases} \quad (8)$$

where $r_G(x)$ and r_β are ERFs for the G protein and β-arrestin-2 pathways, respectively. This function is nonzero in regions where ERFs of both pathways have the same sign. Conversely, the selective activation function is,

$$\mathrm{s}(x) = \begin{cases} \left|r_G(x) - r_\beta(x)\right| & if\ \left(r_G(x) > 0\ and\ \ r_\beta(x) < 0\right)\ or\ \left(r_G(x) < 0\ and\ \ r_\beta(x) > 0\right). \\ 0\ otherwise \end{cases} \quad (9)$$

This function is nonzero in regions where ERFs of both pathways have opposite signs. For each function, we also defined corresponding scores as a numerical integral over the domain: the sum of the function was computed 1,000 evenly spaced points over the domain and multiplied by the spacing.

References

1. Smith, J.S., Lefkowitz, R.J., and Rajagopal, S. (2018). Biased signalling: From simple switches to allosteric microprocessors. Nat. Rev. Drug Discov. *17*, 243–260. 10.1038/nrd.2017.229.

2. Weis, W.I., and Kobilka, B.K. (2018). The Molecular Basis of G Protein–Coupled Receptor Activation. Annu. Rev. Biochem. *87*, 897–919. 10.1146/annurev-biochem-060614-033910.

3. Wingler, L.M., Skiba, M.A., McMahon, C., Staus, D.P., Kleinhenz, A.L.W., Suomivuori, C.-M., Latorraca, N.R., Dror, R.O., Lefkowitz, R.J., and Kruse, A.C. (2020). Angiotensin and

483 biased analogs induce structurally distinct active conformations within a GPCR.
484 Science *367*, 888–892. 10.1126/science.aay9813.

485 4. Panel, N., Vo, D.D., Kahlous, N.A., Hübner, H., Tiedt, S., Matricon, P., Pacalon, J.,
486 Fleetwood, O., Kampen, S., Luttens, A., et al. (2023). Design of Drug Efficacy Guided by
487 Free Energy Simulations of the β_2-Adrenoceptor. Angew. Chem. Int. Ed. *62*,
488 e202218959. 10.1002/anie.202218959.

489 5. Vögele, M., Zhang, B.W., Kaindl, J., and Wang, L. (2023). Is the Functional Response of a
490 Receptor Determined by the Thermodynamics of Ligand Binding? J. Chem. Theory
491 Comput. *19*, 8414–8422. 10.1021/acs.jctc.3c00899.

492 6. Hauser, A.S., Attwood, M.M., Rask-Andersen, M., Schiöth, H.B., and Gloriam, D.E.
493 (2017). Trends in GPCR drug discovery: new agents, targets and indications. Nat. Rev.
494 Drug Discov. *16*, 829–842. 10.1038/nrd.2017.178.

495 7. Whalen, E.J., Rajagopal, S., and Lefkowitz, R.J. (2011). Therapeutic potential of β-
496 arrestin- and G protein-biased agonists. Trends Mol. Med. *17*, 126–139.
497 10.1016/j.molmed.2010.11.004.

498 8. Tan, L., Yan, W., McCorvy, J.D., and Cheng, J. (2018). Biased Ligands of G Protein-
499 Coupled Receptors (GPCRs): Structure–Functional Selectivity Relationships (SFSRs)
500 and Therapeutic Potential. J. Med. Chem. *61*, 9841–9878.
501 10.1021/acs.jmedchem.8b00435.

502 9. Seyedabadi, M., Ghahremani, M.H., and Albert, P.R. (2019). Biased signaling of G
503 protein coupled receptors (GPCRs): Molecular determinants of GPCR/transducer
504 selectivity and therapeutic potential. Pharmacol. Ther. *200*, 148–178.
505 10.1016/j.pharmthera.2019.05.006.

506 10. Faouzi, A., Varga, B.R., and Majumdar, S. (2020). Biased Opioid Ligands. Molecules *25*,
507 4257. 10.3390/molecules25184257.

508 11. De Neve, J., Barlow, T.M.A., Tourwé, D., Bihel, F., Simonin, F., and Ballet, S. (2021).
509 Comprehensive overview of biased pharmacology at the opioid receptors: biased
510 ligands and bias factors. RSC Med. Chem. *12*, 828–870. 10.1039/D1MD00041A.

511 12. Eiger, D.S., Pham, U., Gardner, J., Hicks, C., and Rajagopal, S. (2022). GPCR systems
512 pharmacology: a different perspective on the development of biased therapeutics. Am.
513 J. Physiol.-Cell Physiol. *322*, C887–C895. 10.1152/ajpcell.00449.2021.

514 13. Kelly, E., Sutcliffe, K., Cavallo, D., Ramos-Gonzalez, N., Alhosan, N., and Henderson, G.
515 (2023). The anomalous pharmacology of fentanyl. Br. J. Pharmacol. *180*, 797–812.
516 10.1111/bph.15573.

14. Stanley, T.H. (1992). The history and development of the fentanyl series. J. Pain Symptom Manage. *7*, S3–S7. 10.1016/0885-3924(92)90047-L.

15. Leysen, J.E., Gommeren, W., and Niemegeers, C.J.E. (1983). [3H]sufentanil, a superior ligand for μ-opiate receptors: Binding properties and regional distribution in rat brain and spinal cord. Eur. J. Pharmacol. *87*, 209–225. 10.1016/0014-2999(83)90331-X.

16. Spencer, M.R. (2022). Drug Overdose Deaths in the United States, 2001–202.

17. Wingler, L.M., and Lefkowitz, R.J. (2020). Conformational Basis of G Protein-Coupled Receptor Signaling Versatility. Trends Cell Biol. *30*, 736–747. 10.1016/j.tcb.2020.06.002.

18. Wingler, L.M., Elgeti, M., Hilger, D., Latorraca, N.R., Lerch, M.T., Staus, D.P., Dror, R.O., Kobilka, B.K., Hubbell, W.L., and Lefkowitz, R.J. (2019). Angiotensin Analogs with Divergent Bias Stabilize Distinct Receptor Conformations. Cell *176*, 468-478.e11. 10.1016/j.cell.2018.12.005.

19. Lamichhane, R., Liu, J.J., White, K.L., Katritch, V., Stevens, R.C., Wüthrich, K., and Millar, D.P. (2020). Biased Signaling of the G-Protein-Coupled Receptor β2AR Is Governed by Conformational Exchange Kinetics. Structure *28*, 371-377.e3. 10.1016/j.str.2020.01.001.

20. Imai, S., Yokomizo, T., Kofuku, Y., Shiraishi, Y., Ueda, T., and Shimada, I. (2020). Structural equilibrium underlying ligand-dependent activation of β2-adrenoreceptor. Nat. Chem. Biol. *16*, 430–439. 10.1038/s41589-019-0457-5.

21. Cong et. al., X. (2021). Molecular Insights into the Biased Signaling Mechanism of MOR. Mol. Cell *81*, 4165–4175. https://doi.org/10.1016/j.molcel.2021.07.033.

22. Che, T., and Roth, B.L. (2023). Molecular basis of opioid receptor signaling. Cell *186*, 5203–5219. 10.1016/j.cell.2023.10.029.

23. Li, Z., Liu, J., Dong, F., Chang, N., Huang, R., Xia, M., Patterson, T.A., and Hong, H. (2023). Three-Dimensional Structural Insights Have Revealed the Distinct Binding Interactions of Agonists, Partial Agonists, and Antagonists with the μ Opioid Receptor. Int. J. Mol. Sci. *24*, 7042. 10.3390/ijms24087042.

24. Claff, T., Yu, J., Blais, V., Patel, N., Martin, C., Wu, L., Han, G.W., Holleran, B.J., Van Der Poorten, O., White, K.L., et al. (2019). Elucidating the active δ-opioid receptor crystal structure with peptide and small-molecule agonists. Sci. Adv. *5*, eaax9115. 10.1126/sciadv.aax9115.

25. Zhang, D., Zhao, Q., and Wu, B. (2015). Structural Studies of G Protein-Coupled Receptors. Mol. Cells *38*, 836–842. 10.14348/molcells.2015.0263.

26. Piekielna-Ciesielska, J., Artali, R., Azzam, A.A.H., Lambert, D.G., Kluczyk, A., Gentilucci, L., and Janecka, A. (2020). Pharmacological Characterization of μ-Opioid Receptor Agonists with Biased G Protein or β-Arrestin Signaling, and Computational Study of Conformational Changes during Receptor Activation. Molecules *26*, 13. 10.3390/molecules26010013.

27. Zhuang, Y., Wang, Y., He, B., He, X., Zhou, X.E., Guo, S., Rao, Q., Yang, J., Liu, J., Zhou, Q., et al. (2022). Molecular recognition of morphine and fentanyl by the human μ-opioid receptor. Cell *185*, 4361-4375.e19. 10.1016/j.cell.2022.09.041.

28. Qu, Q., Huang, W., Aydin, D., Paggi, J.M., Seven, A.B., Wang, H., Chakraborty, S., Che, T., DiBerto, J.F., Robertson, M.J., et al. (2023). Insights into distinct signaling profiles of the μOR activated by diverse agonists. Nat. Chem. Biol. *19*, 423–430. 10.1038/s41589-022-01208-y.

29. Faouzi, A., Wang, H., Zaidi, S.A., DiBerto, J.F., Che, T., Qu, Q., Robertson, M.J., Madasu, M.K., El Daibani, A., Varga, B.R., et al. (2023). Structure-based design of bitopic ligands for the μ-opioid receptor. Nature *613*, 767–774. 10.1038/s41586-022-05588-y.

30. Ballesteros, J.A., and Weinstein, H. (1995). [19] Integrated methods for the construction of three-dimensional models and computational probing of structure-function relations in G protein-coupled receptors. In Methods in Neurosciences Receptor Molecular Biology., S. C. Sealfon, ed. (Academic Press), pp. 366–428. 10.1016/S1043-9471(05)80049-7.

31. Suomivuori, C.-M., Latorraca, N.R., Wingler, L.M., Eismann, S., King, M.C., Kleinhenz, A.L.W., Skiba, M.A., Staus, D.P., Kruse, A.C., Lefkowitz, R.J., et al. (2020). Molecular mechanism of biased signaling in a prototypical G protein–coupled receptor. Science *367*, 881–887. 10.1126/science.aaz0326.

32. Black, J.W., and Leff, P. (1983). Operational Models of Pharmacological Agonism. Proc. R. Soc. Lond. B Biol. Sci. *220*, 141–162.

33. Olsen, R.H.J., and English, J.G. (2023). Advancements in G protein-coupled receptor biosensors to study GPCR-G protein coupling. Br. J. Pharmacol. *180*, 1433–1443. 10.1111/bph.15962.

34. Huang, W., Manglik, A., Venkatakrishnan, A.J., Laeremans, T., Feinberg, E.N., Sanborn, A.L., Kato, H.E., Livingston, K.E., Thorsen, T.S., Kling, R.C., et al. (2015). Structural insights into μ-opioid receptor activation. Nature *524*, 315–321. 10.1038/nature14886.

35. Sounier, R., Mas, C., Steyaert, J., Laeremans, T., Manglik, A., Huang, W., Kobilka, B.K., Déméné, H., and Granier, S. (2015). Propagation of conformational changes during μ-opioid receptor activation. Nature *524*, 375–378. 10.1038/nature14680.

36. Mafi, A., Kim, S.-K., and Goddard, W.A. (2020). Mechanism of β-arrestin recruitment by the μ-opioid G protein-coupled receptor. Proc. Natl. Acad. Sci. U. S. A. *117*, 16346–16355. 10.1073/pnas.1918264117.

37. Kelly, B., Hollingsworth, S.A., Blakemore, D.C., Owen, R.M., Storer, R.I., Swain, N.A., Aydin, D., Torella, R., Warmus, J.S., and Dror, R.O. (2021). Delineating the Ligand–Receptor Interactions That Lead to Biased Signaling at the μ-Opioid Receptor. J. Chem. Inf. Model. *61*, 3696–3707. 10.1021/acs.jcim.1c00585.

38. Manglik, A., Lin, H., Aryal, D.K., McCorvy, J.D., Dengler, D., Corder, G., Levit, A., Kling, R.C., Bernat, V., Hübner, H., et al. (2016). Structure-based discovery of opioid analgesics with reduced side effects. Nature *537*, 185–190. 10.1038/nature19112.

39. Wang, H., Hetzer, F., Huang, W., Qu, Q., Meyerowitz, J., Kaindl, J., Hübner, H., Skiniotis, G., Kobilka, B.K., and Gmeiner, P. (2022). Structure-Based Evolution of G Protein-Biased μ-Opioid Receptor Agonists. Angew. Chem. Int. Ed. *61*, e202200269. 10.1002/anie.202200269.

40. Shang, Y., LeRouzic, V., Schneider, S., Bisignano, P., Pasternak, G.W., and Filizola, M. (2014). Mechanistic Insights into the Allosteric Modulation of Opioid Receptors by Sodium Ions. Biochemistry *53*, 5140–5149. 10.1021/bi5006915.

41. Marmolejo-Valencia, A.F., Madariaga-Mazón, A., and Martinez-Mayorga, K. (2021). Bias-inducing allosteric binding site in mu-opioid receptor signaling. SN Appl. Sci. *3*, 566. 10.1007/s42452-021-04505-8.

42. Sutcliffe, K.J., Henderson, G., Kelly, E., and Sessions, R.B. (2017). Drug Binding Poses Relate Structure with Efficacy in the μ Opioid Receptor. J. Mol. Biol. *429*, 1840–1851. 10.1016/j.jmb.2017.05.009.

43. Trzaskowski, B., Latek, D., Yuan, S., Ghoshdastider, U., Debinski, A., and Filipek, S. (2012). Action of Molecular Switches in GPCRs - Theoretical and Experimental Studies. Curr. Med. Chem. *19*, 1090–1109. 10.2174/092986712799320556.

44. Ricarte, A., Dalton, J.A.R., and Giraldo, J. (2021). Structural Assessment of Agonist Efficacy in the μ-Opioid Receptor: Morphine and Fentanyl Elicit Different Activation Patterns. J. Chem. Inf. Model. *61*, 1251–1274. 10.1021/acs.jcim.0c00890.

45. Ravindranathan, A., Joslyn, G., Robertson, M., Schuckit, M.A., Whistler, J.L., and White, R.L. (2009). Functional characterization of human variants of the mu-opioid receptor gene. Proc. Natl. Acad. Sci. *106*, 10811–10816. 10.1073/pnas.0904509106.

46. Dolinsky, T.J., Czodrowski, P., Li, H., Nielsen, J.E., Jensen, J.H., Klebe, G., and Baker, N.A. (2007). PDB2PQR: expanding and upgrading automated preparation of biomolecular structures for molecular simulations. Nucleic Acids Res. *35*, W522–W525. 10.1093/nar/gkm276.

47. Lomize, A.L., Pogozheva, I.D., and Mosberg, H.I. (2011). Anisotropic Solvent Model of the Lipid Bilayer. 2. Energetics of Insertion of Small Molecules, Peptides, and Proteins in Membranes. J. Chem. Inf. Model. *51*, 930–946. 10.1021/ci200020k.

48. Maier, J.A., Martinez, C., Kasavajhala, K., Wickstrom, L., Hauser, K.E., and Simmerling, C. (2015). ff14SB: Improving the Accuracy of Protein Side Chain and Backbone Parameters from ff99SB. J. Chem. Theory Comput. *11*, 3696–3713. 10.1021/acs.jctc.5b00255.

49. Izadi, S., Anandakrishnan, R., and Onufriev, A.V. (2014). Building Water Models: A Different Approach. J. Phys. Chem. Lett. *5*, 3863–3871. 10.1021/jz501780a.

50. Case, D.A., Aktulga, H.M., Belfon, K., Cerutti, D.S., Cisneros, G.A., Cruzeiro, V.W.D., Forouzesh, N., Giese, T.J., Götz, A.W., Gohlke, H., et al. (2023). AmberTools. J. Chem. Inf. Model. *63*, 6183–6191. 10.1021/acs.jcim.3c01153.

51. Eastman, P., Swails, J., Chodera, J.D., McGibbon, R.T., Zhao, Y., Beauchamp, K.A., Wang, L.-P., Simmonett, A.C., Harrigan, M.P., Stern, C.D., et al. (2017). OpenMM 7: Rapid development of high performance algorithms for molecular dynamics. PLOS Comput. Biol. *13*, e1005659. 10.1371/journal.pcbi.1005659.

52. Boerner, T.J., Deems, S., Furlani, T.R., Knuth, S.L., and Towns, J. (2023). ACCESS: Advancing Innovation: NSF's Advanced Cyberinfrastructure Coordination Ecosystem: Services & Support. In Practice and Experience in Advanced Research Computing (ACM), pp. 173–176. 10.1145/3569951.3597559.

53. Zhang, R., and Xie, X. (2012). Tools for GPCR drug discovery. Acta Pharmacol. Sin. *33*, 372–384. 10.1038/aps.2011.173.

54. Pedregosa, F., Varoquaux, G., Gramfort, A., Michel, V., Thirion, B., Grisel, O., Blondel, M., Prettenhofer, P., Weiss, R., Dubourg, V., et al. (2011). Scikit-learn: Machine Learning in {P}ython. J. Mach. Learn. Res. *12*, 2825–2830.

55. Virtanen, P., Gommers, R., Oliphant, T.E., Haberland, M., Reddy, T., Cournapeau, D., Burovski, E., Peterson, P., Weckesser, W., Bright, J., et al. (2020). SciPy 1.0: fundamental algorithms for scientific computing in Python. Nat. Methods *17*, 261–272. 10.1038/s41592-019-0686-2.

56. van der Walt, S., Colbert, S.C., and Varoquaux, G. (2011). The NumPy Array: A Structure for Efficient Numerical Computation. Comput. Sci. Eng. *13*, 22–30. 10.1109/MCSE.2011.37.

57. Zhou, Y., Ramsey, S., Provasi, D., El Daibani, A., Appourchaux, K., Chakraborty, S., Kapoor, A., Che, T., Majumdar, S., and Filizola, M. (2021). Predicted Mode of Binding to and Allosteric Modulation of the μ-Opioid Receptor by Kratom's Alkaloids with

Reported Antinociception *In Vivo*. Biochemistry *60*, 1420–1429. 10.1021/acs.biochem.0c00658.

58. Schmid, C.L., Kennedy, N.M., Ross, N.C., Lovell, K.M., Yue, Z., Morgenweck, J., Cameron, M.D., Bannister, T.D., and Bohn, L.M. (2017). Bias Factor and Therapeutic Window Correlate to Predict Safer Opioid Analgesics. Cell *171*, 1165-1175.e13. 10.1016/j.cell.2017.10.035.

59. De Waal, P.W., Shi, J., You, E., Wang, X., Melcher, K., Jiang, Y., Xu, H.E., and Dickson, B.M. (2020). Molecular mechanisms of fentanyl mediated β-arrestin biased signaling. PLOS Comput. Biol. *16*, e1007394. 10.1371/journal.pcbi.1007394.

60. Gillis, A., Gondin, A.B., Kliewer, A., Sanchez, J., Lim, H.D., Alamein, C., Manandhar, P., Santiago, M., Fritzwanker, S., Schmiedel, F., et al. (2020). Low intrinsic efficacy for G protein activation can explain the improved side effect profiles of new opioid agonists. Sci. Signal. *13*, eaaz3140. 10.1126/scisignal.aaz3140.

61. Li, X., Guo, Y., Li, J., Yu, Z., Cheng, J., Ren, F., Jia, H., Zhang, Y., Cui, S., Zhang, T., et al. (2022). Discovery and Structural Explorations of G-Protein Biased μ-Opioid Receptor Agonists. ChemMedChem *17*. 10.1002/cmdc.202200416.

62. Gutridge, A.M., Robins, M.T., Cassell, R.J., Uprety, R., Mores, K.L., Ko, M.J., Pasternak, G.W., Majumdar, S., and Van Rijn, R.M. (2020). G protein-biased kratom-alkaloids and synthetic carfentanil-amide opioids as potential treatments for alcohol use disorder. Br. J. Pharmacol. *177*, 1497–1513. 10.1111/bph.14913.

Acknowledgments

This work used CPU and GPU Nodes at SDSC Expanse and PSC Bridges2 through allocation BIO230006 from the Advanced Cyberinfrastructure Coordination Ecosystem: Services & Support (ACCESS) program, which is supported by National Science Foundation grants #2138259, #2138286, #2138307, #2137603, and #2138296. We thank Bob Eisenberg for comments on the manuscript.

Funding

National Institutes of Health grant R01GM127712 (DDLM)

Author contributions

Conceptualization: DDLM, DAC, JDB, SN, BG

Methodology: DDLM, DAC, JDB

Investigation: DDLM, DAC

Visualization: DDLM, DAC

Funding acquisition: DDLM

Project administration: DDLM

Supervision: DDLM

Writing – original draft: DAC, DDLM

Writing – review & editing: DDLM, DAC, JDB

Competing interests

DAC and DDLM are co-inventors of the methodology described in this work and the Illinois Institute of Technology has filed a provisional patent on their behalf. They have started a company, Biagon Inc., to commercialize the technology.

Figure Legends

Figure 1 Signaling efficacy predictions of ligands for (**A**) G protein and (**B**) β-arrestin-2 pathways. On the x axis, each predicted efficacy (relative to DAMGO) is based on a model trained using all other ligands. The error bar is the standard deviation across 11 cross validation models. On the y axis, each experimental efficacy is the median of reported values listed in Table S1. Error bars are standard deviations of these values. Abbreviations: DAM: DAMGO, FEN: fentanyl, LFT: lofentanil, MPH: morphine, TRV: TRV130, SR: SR17018, PZM: PZM21, FH: FH210, C5:

c5guano, C6: c6guano, MP: mitragynine pseudoindoxyl. Efficacies are percentages relative to DAMGO.

Figure 1 Multiple linear regression slopes of each conformation. The mean (markers) and standard deviation (error bars) are of slopes across all 11 cross validation models.

Figure 3 Alpha carbon distances with the largest (A) general and (B) selective activation scores. Structures are medoids of conformations from the machine learning model, colored by different types of activity: high (cyan, conformation 1), low (grey, conformation 14), G protein (green, conformation 4), and β-arrestin-2 (pink, conformation 2). They are shown from the membrane perspective facing the intracellular pocket. Dashed lines are between atoms are shown for the top 2% of activation function scores. For a full table of general and selective activation scores for alpha carbon distances, see Fig. S5.

Figure 4 Amino acid positions containing dihedral angles with the highest general and selective activation scores. Structures are medoids of conformations from the machine learning model, colored by different types of activity: high (cyan, conformation 1), low (grey, conformation 14), G protein (green, conformation 4), and β-arrestin-2 (pink, conformation 2). Displayed amino acids contain dihedral angles in the top two percent of general (**A**, **B**) activation scores or (**C**, **D**) selective activation scores. Side chain rotations were adjusted to match the degree with the highest value of the (A, B) general or (C, D) selective activation function. Views of the binding pocket (A, C) are from the perspective behind the binding pocket region of TM7. TM1 and TM7 (A) and TM6 and TM7 (C) were removed to improve the display of binding pocket amino acids. Views of the intracellular region are from the perspective behind TM3 (B) and TM7 (D). TM3 (B), TM6 and TM7 (D) are removed to clearly display the intracellular amino acids. A comprehensive table of

727 general activation and selective activation function scores for analyzed residues are shown in Fig.
728 S9 and 10, respectively.

729 **Figure 5 Distances in the sodium binding pocket with the highest general and selective**
730 **activation scores.** Structures are medoids of conformations from the machine learning model. (**A**)
731 Distances between OD1 of D116$^{2.50}$ and ND2 of N334$^{7.49}$ in structures with high (cyan,
732 conformation 1) and low (grey, conformation 14) activity. (**B**) Distances between OD2 of D116$^{2.50}$
733 and ND2 of N330$^{7.49}$ in conformations with high G protein (green, conformation 4) and β-arrestin-
734 2 (pink, conformation 2) activity. TM5 is removed to improve display of amino acid distances in
735 the sodium binding pocket. A comprehensive listing of general activation and selective activation
736 function scores for analyzed polar residue distances is shown in Fig. S10.

737

Supplementary Material

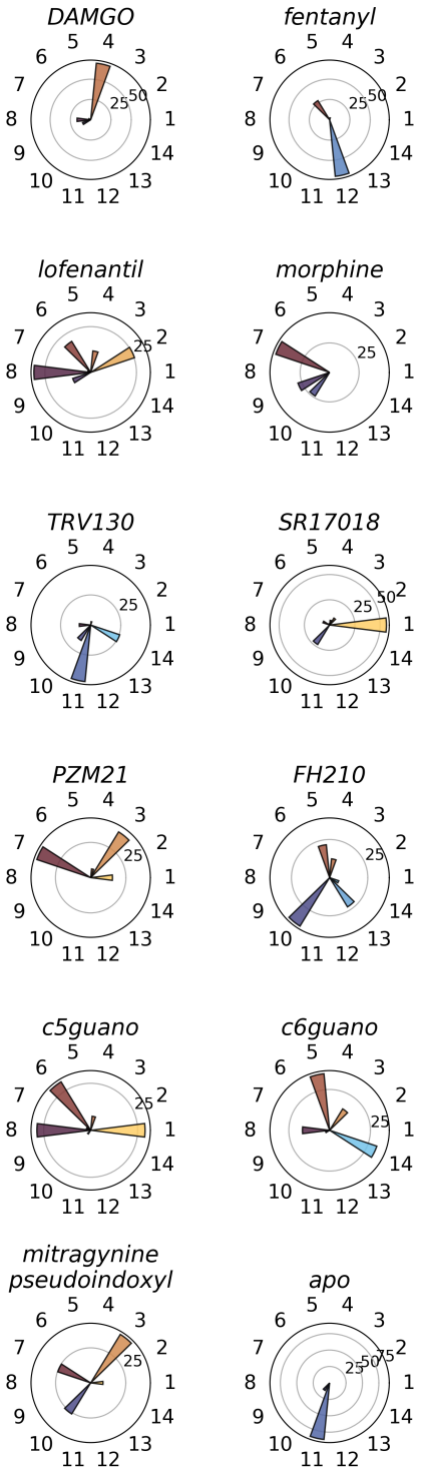

Figure S1 Percentages of simulations of complexes with different ligands in each conformation.

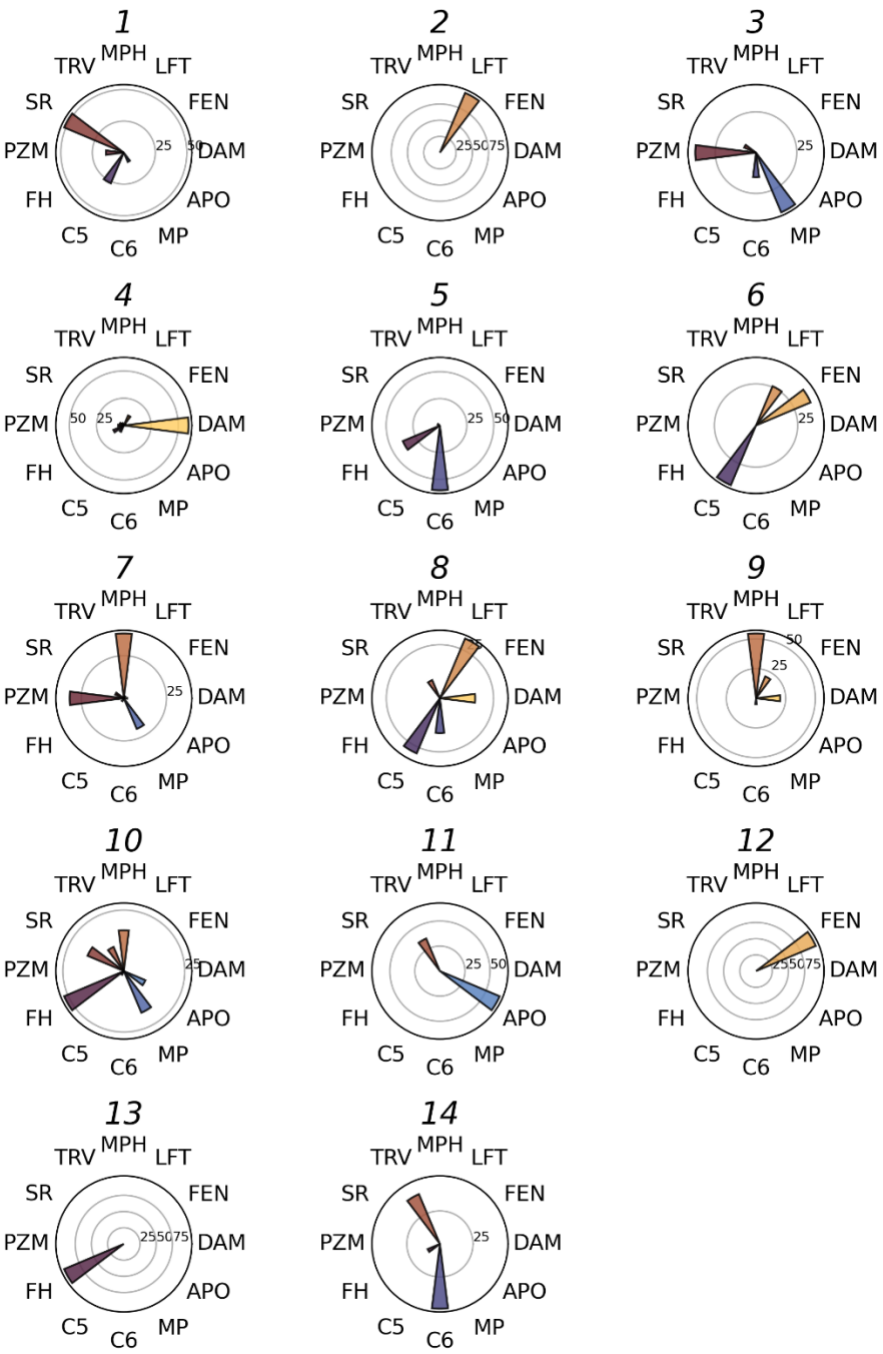

Figure S2 Percentage of conformations accessed in simulations with each complex**.** Abbreviations: DAM: DAMGO, FEN: fentanyl, LFT: lofentanil, MPH: morphine, TRV: TRV130, SR: SR17018, PZM: PZM21, FH: FH210, C5: c5guano, C6: c6guano, MP: mitragynine pseudoindoxyl, APO: apo.

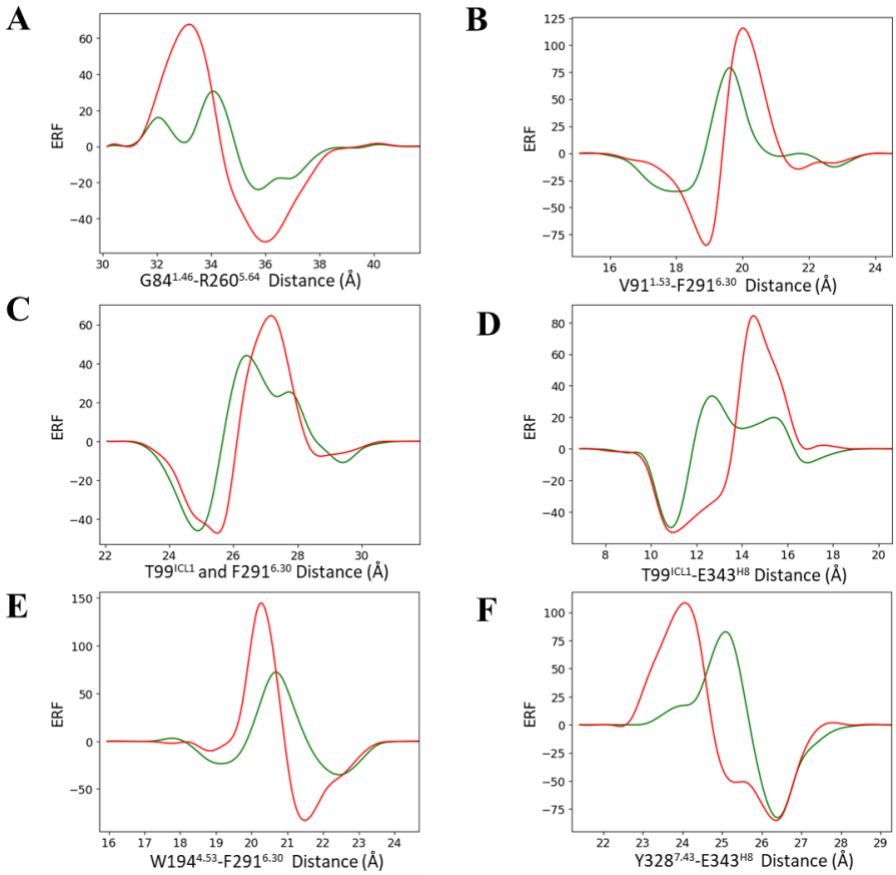

Figure S3 Efficacy response functions for alpha carbon distances with the largest general activation scores: **(A)** G84$^{1.46}$-R260$^{5.64}$**, (B)** V91$^{1.53}$-F291$^{6.30}$, **(C)** T99^{ICL1}-F291$^{6.30}$, **(D)** T99^{ICL1}-E343^{H8}, **(E)** W194$^{4.53}$-F291$^{6.30}$, and **(F)** Y328$^{7.43}$-E343^{H8}. The green and red curves correspond to the G protein and β-arrestin-2 efficacy response functions (ERF), respectively.

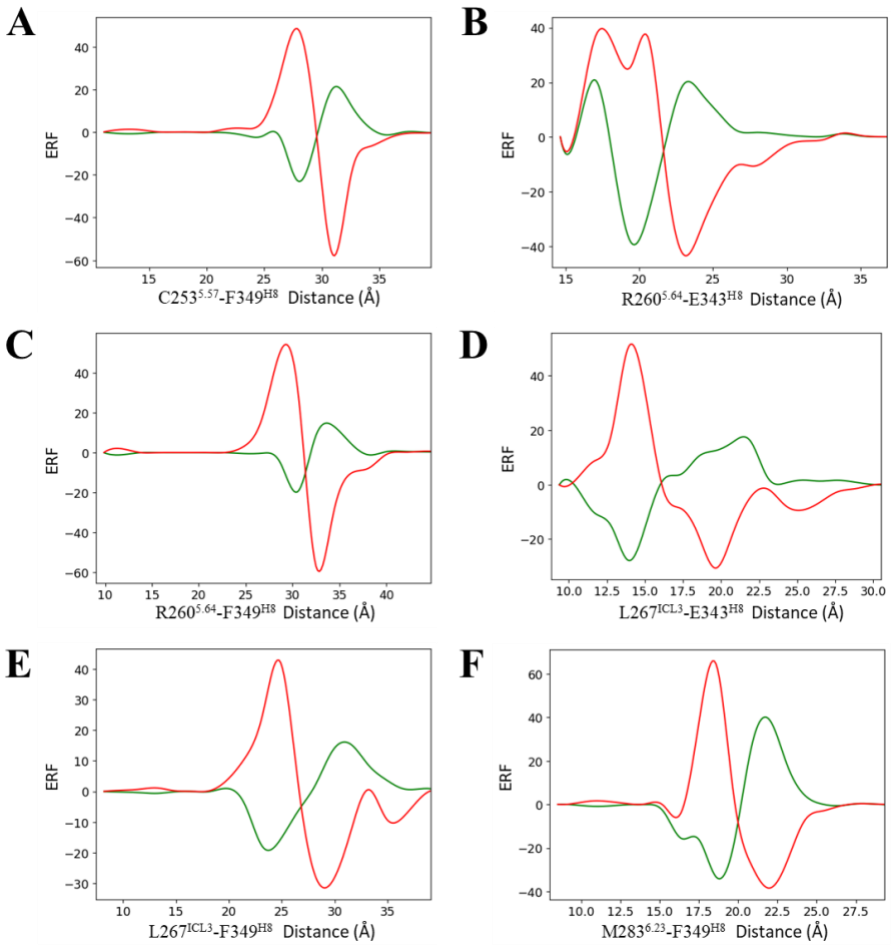

Figure S4 Efficacy response functions for alpha carbon distances with the largest selective activation scores: **(A)** C253$^{5.57}$-F349^{H8}, **(B)** R260$^{5.64}$-E343^{H8}, **(C)** R260$^{5.64}$-F349^{H8}, **(D)** L267^{ICL3}-E343^{H8}, **(E)** L267^{ICL3}-F349^{H8}, and (**F**) M283$^{6.23}$-F349^{H8}. The green and red curves correspond to the G protein and β-arrestin-2 efficacy response functions (ERF), respectively.

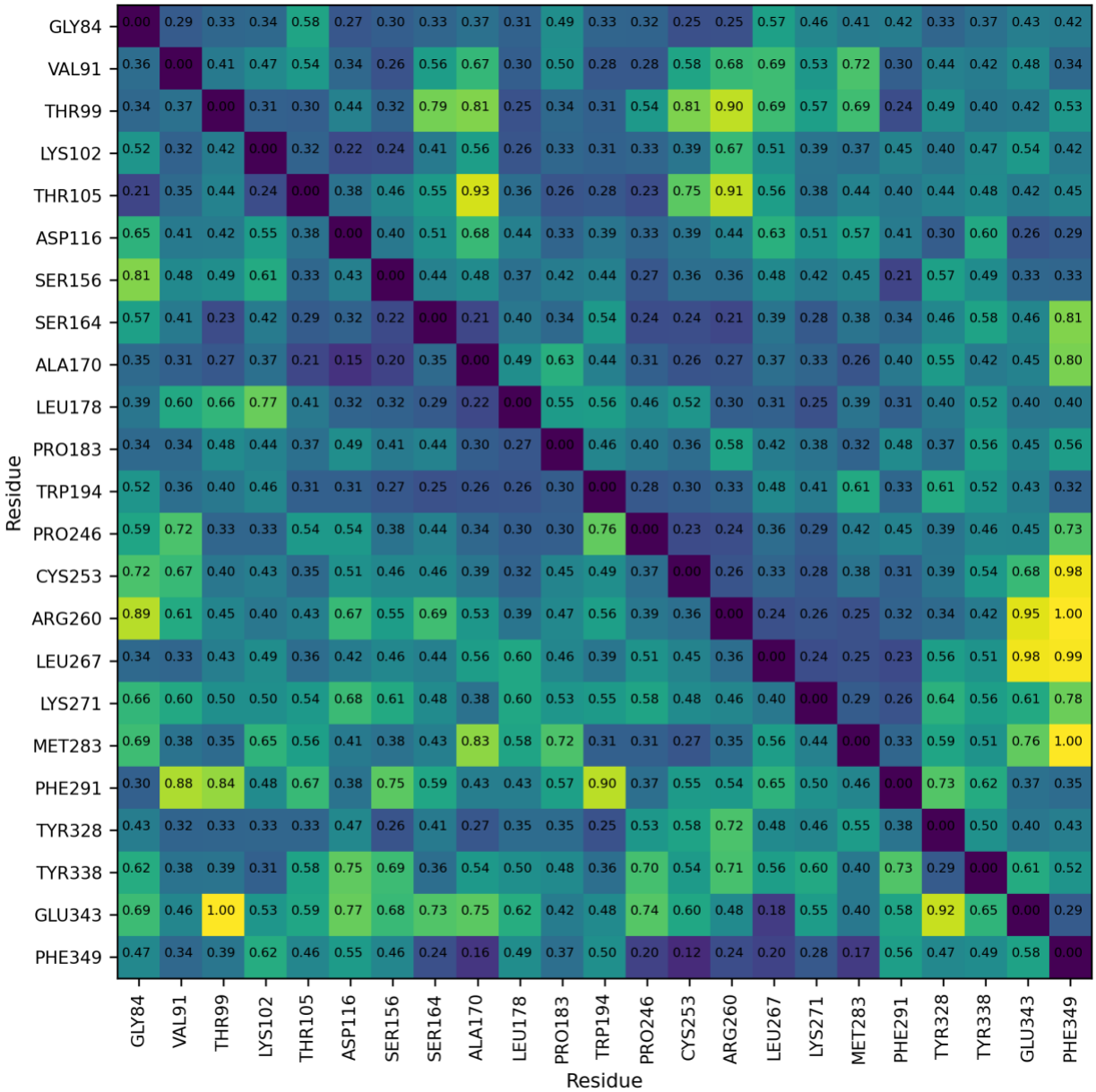

Figure S5 Efficacy response function scores for pairwise distances between alpha carbons from residues in the middle and intracellular end of each helix, with at least one residue in between, and the middle of each intracellular loop. Scores below the diagonal were calculated with the general activation function (Equation 8). Scores above the diagonal were calculated with the selective activation function (Equation 9). Scores from each category were divided by the largest score in the category.

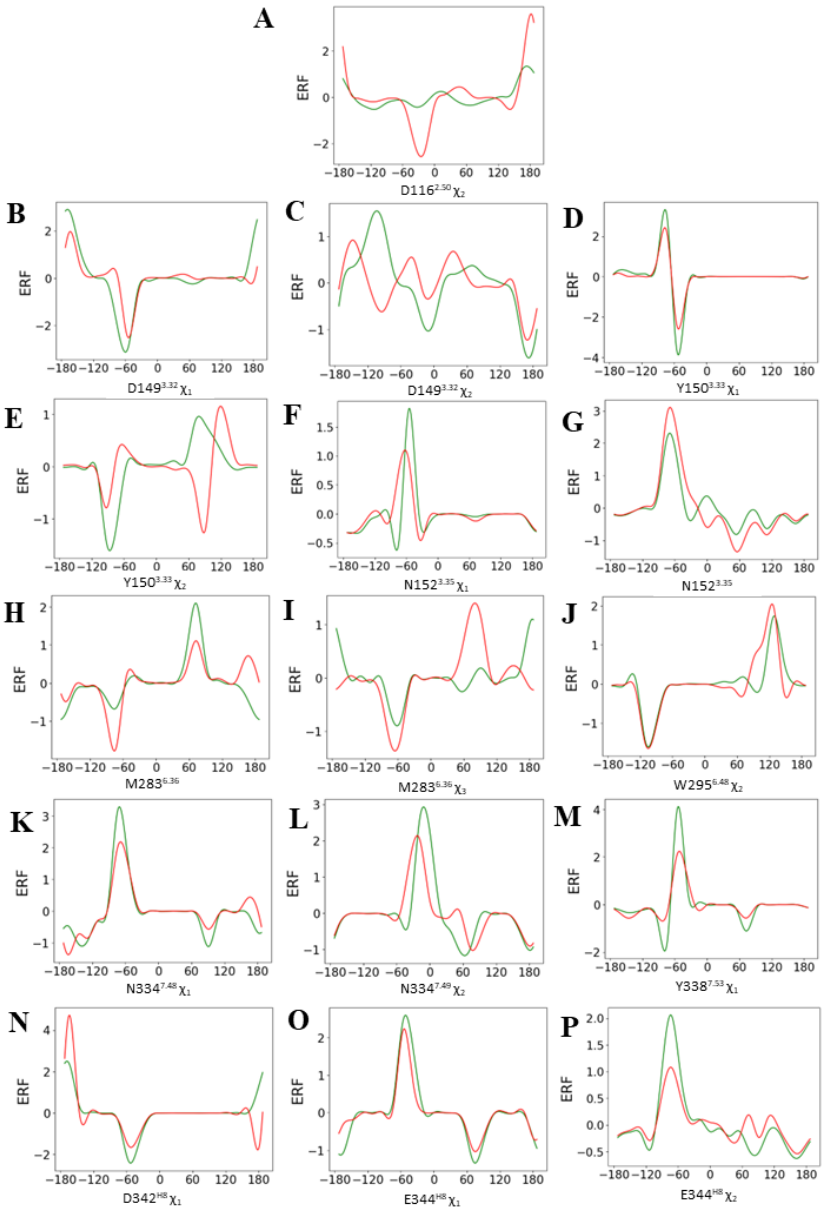

Figure S6 Efficacy response functions for dihedral angles with the largest general activation scores**: (A)** D116$^{2.50}$ χ_2 angle, **(B)** D149$^{3.32}$ χ_1 angle, **(C)** D149$^{3.32}$ χ_2 angle, **(D)** Y150$^{3.33}$ χ_1 angle, **(E)** Y150$^{3.33}$ χ_2 angle, **(F)** N152$^{3.35}$ χ_1 angle, **(G)** N152$^{3.35}$ χ_2 angle, **(H)** M283$^{6.36}$ χ_2 angle, **(I)** M283$^{6.36}$ χ_3 angle, **(J)** W295$^{6.48}$ χ_2 angle, **(K)** N334$^{7.48}$ χ_1 angle, **(L)** N334$^{7.49}$ χ_2 angle, **(M)** Y338$^{7.53}$ χ_1 angle, **(N)** D342^{H8} χ_1 angle**, (O)** E344^{H8} χ_1 angle, **(P)** E344^{H8} χ_2 angle. The green and red curves correspond to the G protein and β-arrestin-2 efficacy response functions (ERF), respectively.

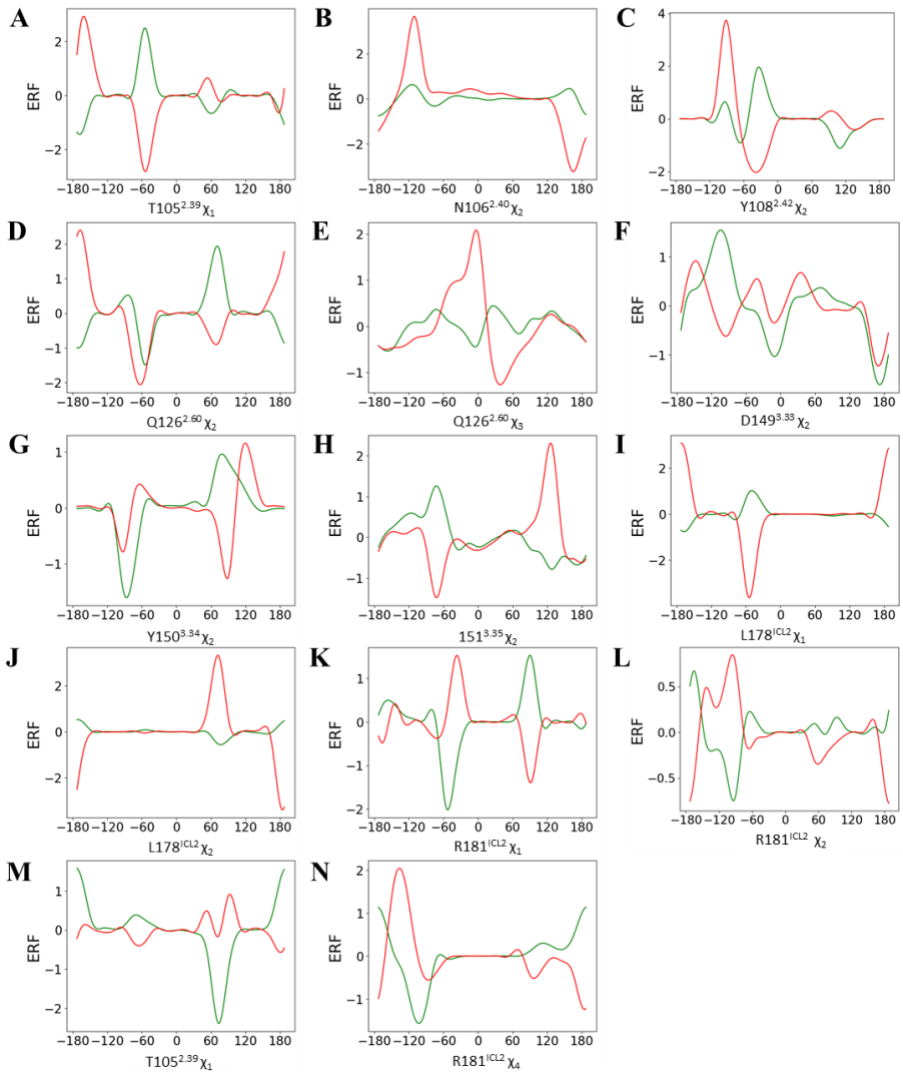

Figure S7 Efficacy response functions for dihedral angles with the largest selective activation scores**: (A)** T105$^{2.39}$ χ_1 angle, **(B)** N106$^{2.40}$ χ_2 angle, **(C)** Y108$^{2.42}$ χ_2 angle, **(D)** Q126$^{2.60}$ χ_2 angle, **(E)** Q126$^{2.60}$ χ_3 angle, **(F)** D149$^{3.32}$ χ_2 angle, **(G)** Y150$^{3.33}$ χ_2 angle, **(H)** 151$^{3.35}$ χ_2 angle, **(I)** L178^{ICL2} χ_1 angle, **(J)** L178^{ICL2} χ_2 angle, **(K)** R181^{ICL2} χ_1 angle, **(L)** R181^{ICL2} χ_2 angle, **(M)** R181^{ICL2} χ_3 angle, **(N)** R181^{ICL2} χ_4 angle. The green and red curves correspond to the G protein and β-arrestin-2 efficacy response functions (ERF), respectively.

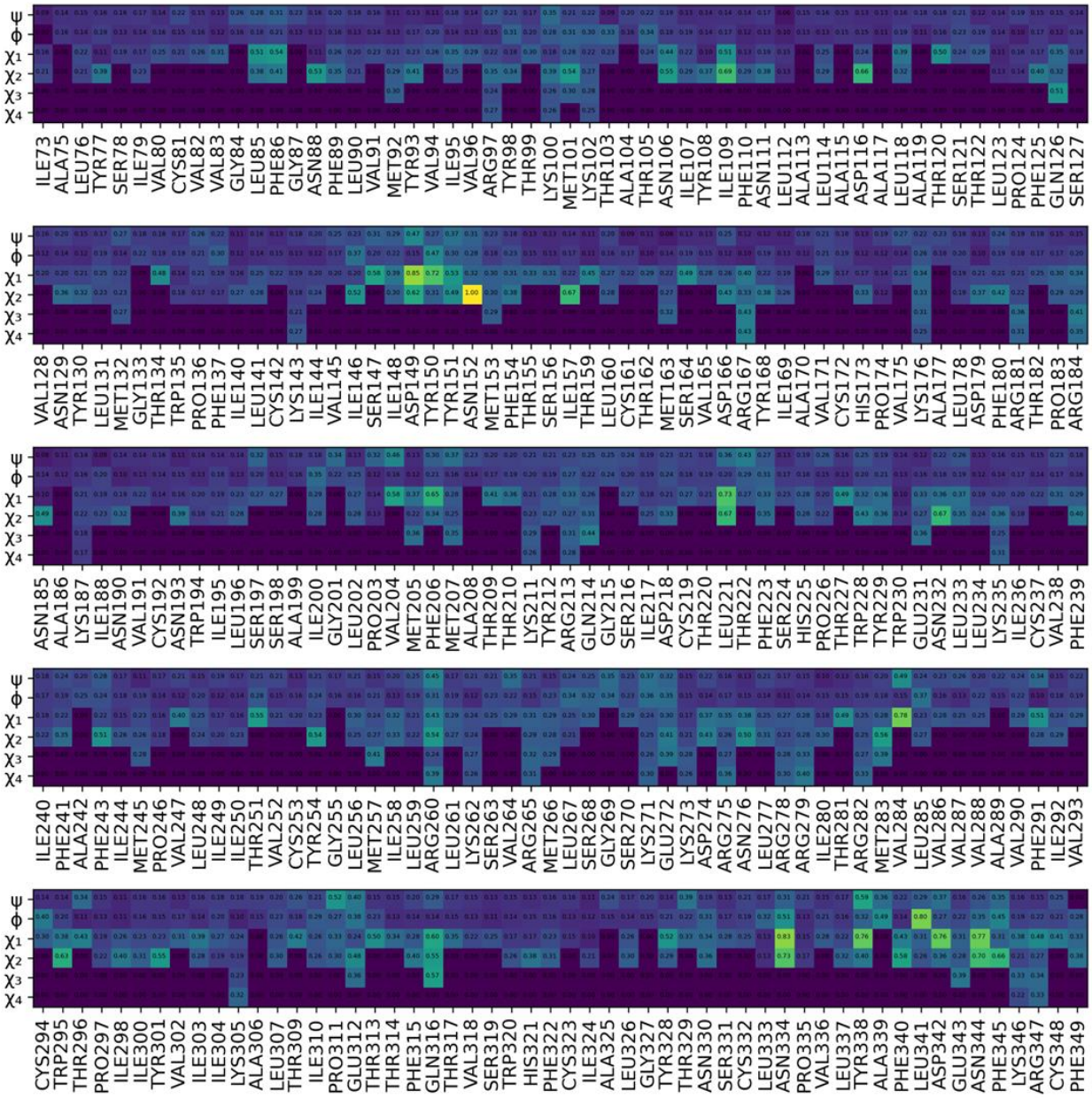

Figure S9 General activation function scores for amino acid dihedral angles.

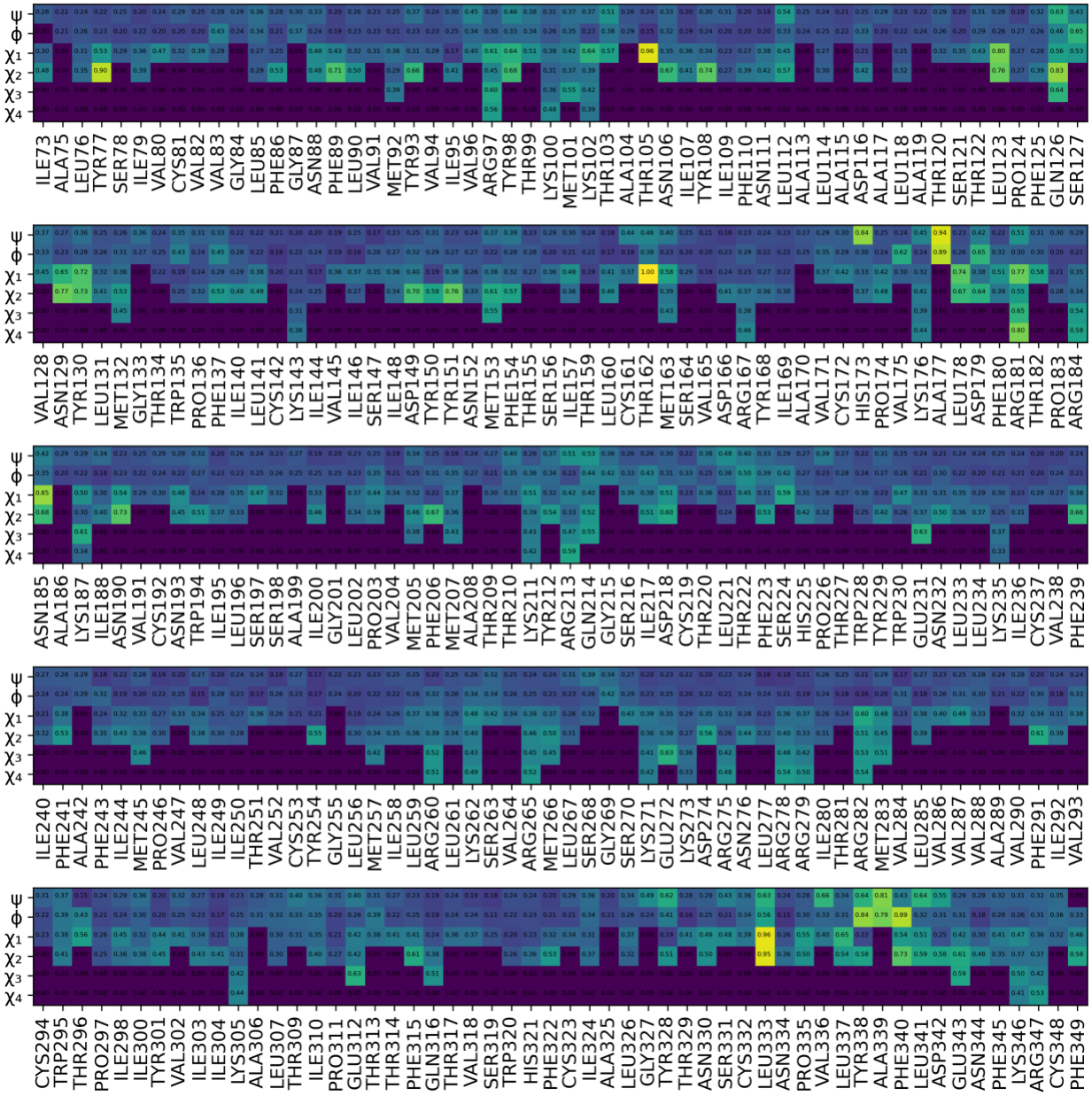

Figure S10 Selective activation function scores for amino acid dihedral angles.

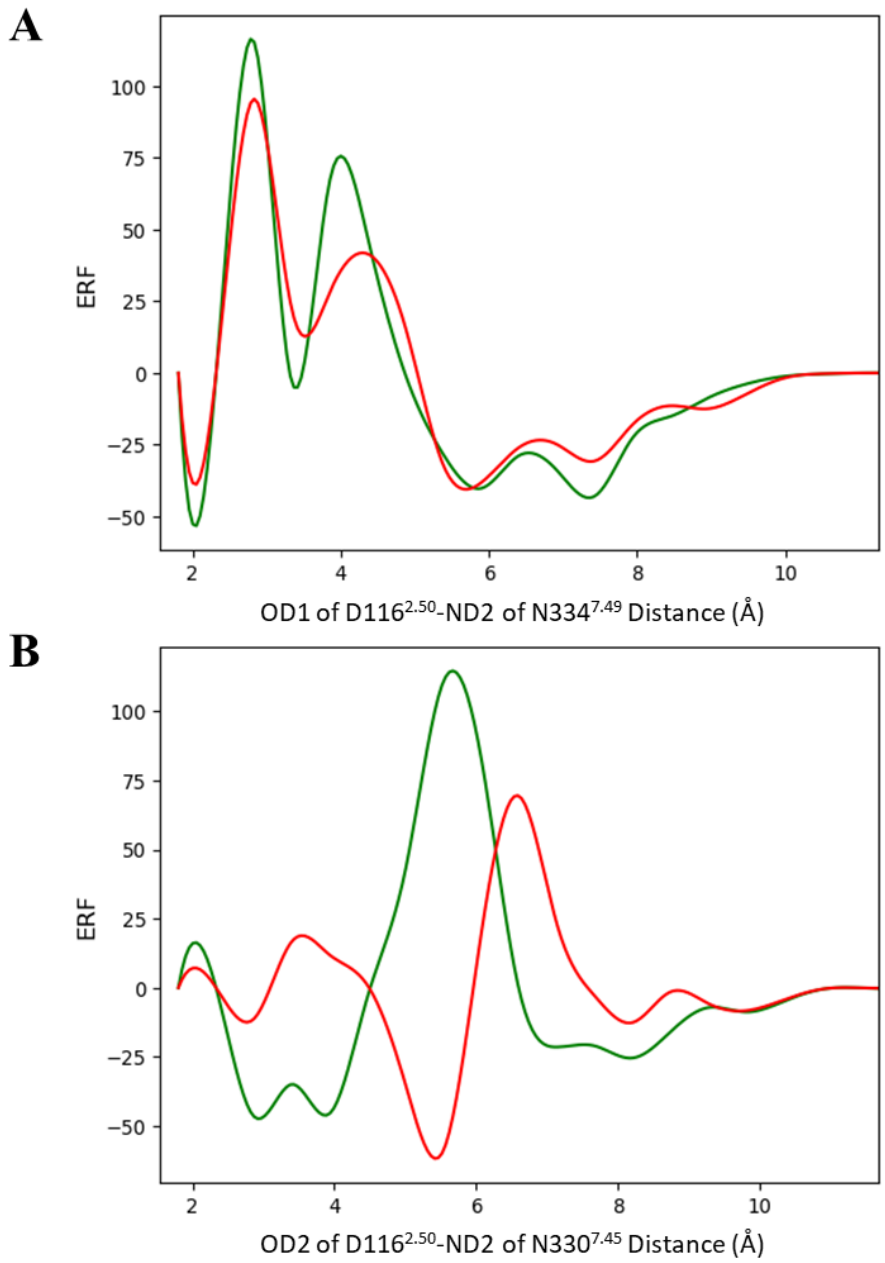

Figure S11 Efficacy response functions of the distance between sodium pocket polar atoms**:** (**A)** OD1 of D116$^{2.50}$ and ND2 of N334$^{7.49}$ and (**B)** OD2 of D116$^{2.50}$ and ND2 of N330$^{7.45}$. The green and red curves correspond to the G protein and β-arrestin-2 efficacy response functions (ERF), respectively.

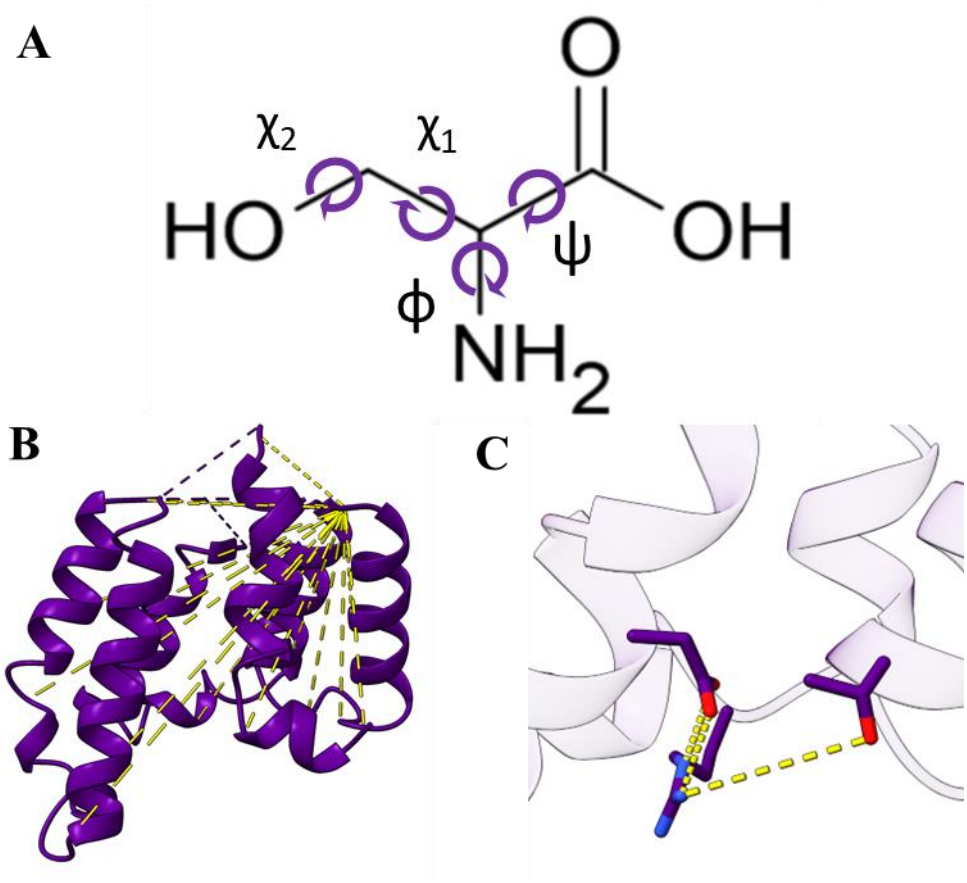

Figure S12 Representatives of features used to discretize configurations into conformations: **A)** dihedral angles, **B)** alpha carbon distances, and **C)** distances between polar atoms in the intracellular region of the μOR.

Ligand	Structure	PDBID	G protein E_{max}	β-arr-2 E_{max}	Sources
FH210	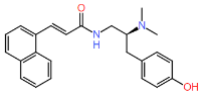	7scg	80 (4)*	18 (2)*	[39]
mitragynine pseudoindoxyl	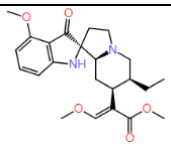	7t2g	81 (4)	0 (0)**	[57]
lofentanil	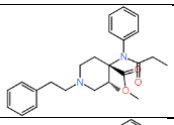	7t2h	115 (2)***	110 (3)	[28]
c6guano	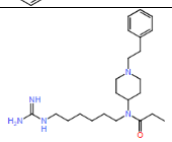	7u2k	137 (2)	19 (1)	[29]
c5guano	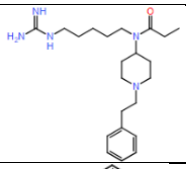	7u2l	104 (3)	54 (3)	[29]
fentanyl	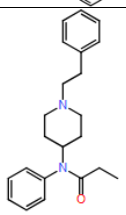	8ef5	92 (4)	60 (2)	[27,29,58–60]
morphine	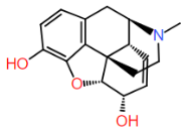	8ef6	97 (4)	28 (3)	[27,38,58,60,61]
TRV130	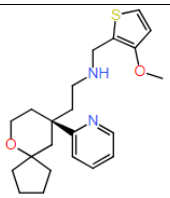	8efb	86 (8)	0 (0)**	[27,38,60,62]
SR10718	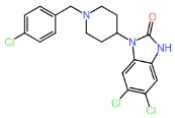	8efl	62 (12)	12 (1)	[27,58,60]
PZM21	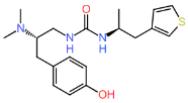	8efo	91 (7)	0 (0)**	[27,38,60,61]
DAMGO	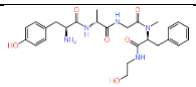	8efq	100	100	

** Converted to DAMGO reference from median experimental reference*
*** Not detectable*
**** Average across multiple Gα subtypes*

Table S1: Summary of structures and efficacy data used for MDS and model training. Emax reported as median Emax (median STD)

Ligand	G protein Recruitment (% of DAMGO)	Uncertainty	Assay	β-arrestin-2 recruitment (% of DAMGO)	Uncertainty	Assay	Source
MP	81	4	cAMP			NR	[57]
TRV130	66	2	cAMP	ND	ND	BRET	[38]
	86	3	cAMP	ND	ND	PathHunter	[62]
	86	5	cAMP	16	3	FRET	[60]
	86	6	cAMP	ND	ND	NanoBit	[27]
PZM21	76	3	cAMP	ND	ND	BRET	[38]
	84	7	cAMP	14	3	BRET	[60]
	97	NR	cAMP	ND	ND	NanoBit	[61]
	112	8	cAMP	ND	ND	NanoBit	[27]
SR17018	105	3	cAMP	10	6	PathHunter	[58]
	62	12	cAMP	12	1	BRET	[60]
	49	12	cAMP	13	5	NanoBit	[27]
Morphine	100	NR	cAMP	14	NR	NanoBit	[61]
	97	1	cAMP	24	1	PathHunter	[58]
	97	4	cAMP	28	3	BRET	[60]
	107	4	cAMP	29	1	NanoBit	[27]
	89	2	cAMP	39	6	BRET	[38]
Fentanyl	97	5	cAMP	60	2	PathHunter	[58]
	NR	NR	NR	59	NR	NanoBit	[59]
	87	4	cAMP	43	4	NanoBit	[27]
	86	2	cAMP	119	3	Tango	[29]
	100	5	cAMP	70	4	NanoBit	[60]
LFT	115	2	BRET	110	3	BRET	[28]
c5guano	104	3	cAMP	54	3	Tango	[29]
c6guano	137	2	cAMP	19	1	Tango	[29]
FH210	80*	4	IP-One	18*	2	PathHunter	[39]

NR Not reported

ND Not detectable

* Converted to DAMGO reference from median experimental reference

Table S2: Experimental cAMP and β-arrestin-2 efficacies used to compute the median experimental efficacies for model training.